CMS Conference Report

January 15, 1999

Calorimetry

T.S. Virdee

CERN, Geneva, Switzerland and Imperial College of Science, Technology and Medicine, London, UK

CMS Collaboration

Abstract

These lectures deal with calorimeters and rely heavily on previous reviews of calorimetry [1-6]. The emphasis is placed on their use at the future Large Hadron Collider and examples from ATLAS [7] and CMS [8] are extensively used.

Presented at Techniques and Concepts of High Energy Physics,
St Croix, Virgin Islands, USA, June 1998

CALORIMETRY

Tejinder S. Virdee

EP Division, CERN and

Imperial College of Science Technology and Medicine, London, UK

1. INTRODUCTION

The aim of Particle Physics is to answer the two following questions: what are the fundamental constituents of matter? and what are the fundamental forces that control their behaviour at the most basic level? Experimentally this involves the study of hard particle interactions, determining the identity of the resulting particles and measuring their momenta with as high a precision as possible. Some thirty years ago a single detection device, the bubble chamber, was sufficient to reconstruct the full event information. At the current high centre of mass energies no single detector can accomplish this even though the number of particles whose identity and momenta need to be determined is limited [electrons, muons, photons, single charged hadrons, jets of hadrons, b-jets, taus and missing transverse energy $E_t(\nu)$]. This leads to a familiar onion-like structure of present day high energy physics experiments.

Starting from the interaction vertex the momenta (and sometimes the identity) of charged particles is determined in the inner tracker which is usually immersed in a solenoidal magnetic field. Identification of b-jets can be accomplished by placing high spatial resolution detectors such as Si pixel or microstrip detectors close to the interaction point. Following the tracking detectors are calorimeters which measure the energies, and identity, of electrons, photons, single hadrons or jets of hadrons. With the absorption of these particles only muons and neutrinos penetrate through the calorimeters. The muons are identified and measured in the outermost sub-detector, the muon system, which is usually immersed in a magnetic field. The presence of neutrinos is deduced from the apparent imbalance of transverse momentum or energy.

These lectures deal with calorimeters and rely heavily on previous reviews of calorimetry [1-6]. The emphasis is placed on their use at the future Large Hadron Collider and examples from ATLAS [7] and CMS [8] are extensively used.

2. CALORIMETRY

Neutral and charged particles incident on a block of material deposit their energy through creation and destruction processes. An example of such phenomena is illustrated in Figure 1 in which a 50 GeV electron is incident on the BEBC Ne/H$_2$ (70%/30%) bubble chamber in a 3 T magnetic field. The deposited energy is rendered measurable by ionisation or excitation of the atoms of matter in the active medium. The active medium can be the block itself (*totally active or homogeneous calorimeter*) or a sandwich of dense absorber and light active planes (*sampling calorimeter*). The measurable signal is usually linearly proportional to the incident energy.
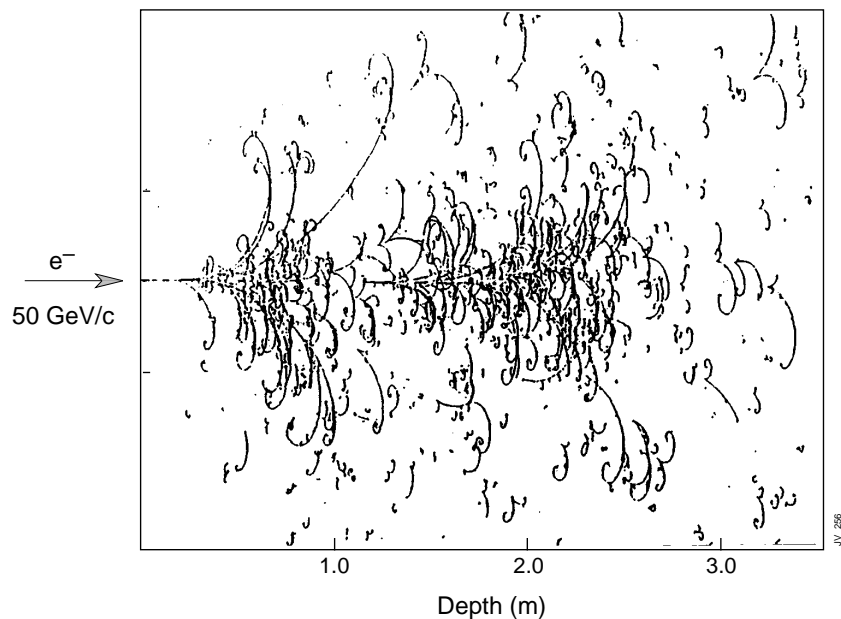

Figure 1: An example of a 50 GeV electron shower in a Ne/H$_2$ (70%/30) filled BEBC bubble chamber. The radiation length is ≈ 34 cm.

Calorimeters are key detectors in present-day experiments for the following reasons:
1   Calorimeters can measure energies of both neutral and charged particles.
2   The absorption of energy of incident particles is via a cascade process that leads to a number of secondary particles, *n*, where *n* is proportional to the incident energy. The cascade development is statistical in nature and the uncertainty on the measurement of energy (σ) is governed by the statistical fluctuation on *n*. Hence the relative energy resolution improves with energy as *$\sigma/E \propto 1/\sqrt{n} = 1/\sqrt{E}$*. This contrasts with momentum measurement of charged particles with tracking devices (in a magnetic field) where the relative momentum resolution dp/p worsens

with increasing p.

3. The longitudinal depth required to contain the cascades only increases logarithmically whereas for magnetic spectrometers the size scales as √p for a constant dp/p.

4. Calorimeters are essentially the only devices that can measure the energies of jets. More emphasis is now placed on the measurement of global characteristics such as jets and missing transverse energy. These arise from processes occurring at the constituent level.

5. Full geometric coverage enables the determination of missing transverse energy, which, if significant, signals the presence of weakly interacting particles such as neutrinos.

6. The cascade develops differently, longitudinally and laterally, for electrons/photons, hadrons and muons. This difference can be exploited to determine the identity of particles.

7. Calorimeters are devices with potentially fast response.

8. The pattern of energy deposit in a calorimeter with good lateral and longitudinal segmentation allows fast, efficient and very selective triggering on e/γ, jets and missing transverse energy.

3. INTERACTION WITH MATTER

3.1 Energy Loss by Charged Particles

Moderately relativistic charged particles, other than electrons, lose energy in matter through the Coulomb interaction with the atomic electrons. The energy transferred to the electrons causes them either to be ejected from the parent atom (*ionisation*) or to be excited to a higher level (*excitation*). The energy loss is given by the Bethe-Bloch equation :

$$-\frac{dE}{dx}\Big|_{ion} = N_A \frac{Z}{A} \frac{4\pi\alpha^2(\hbar c)^2}{m_e c^2} \frac{Z_i^2}{\beta^2} \left[\ln \frac{2m_e c^2 \gamma^2 \beta^2}{I} - \beta^2 - \frac{\delta}{2} \right] \quad \textbf{(1)}$$

where E is the kinetic energy of the incident particle with velocity β and charge Z_i, I ($\approx 10 \times Z$ eV) is the mean ionization potential in a medium with atomic number Z. A very useful quantity is *areal density* measured in units of $g.cm^{-2}$. The energy loss of relativistic particles of unit electric charge per unit areal density is found to be roughly the same in all materials with

$$\frac{1}{\rho}\frac{dE}{dx} \approx 1.5 - 2 \frac{MeV}{g.cm^{-2}}$$

where ρ is the density of the medium. The energy loss rate in liquid hydrogen, gaseous helium, carbon, aluminium, tin and lead is shown in Figure 2 [9]. It can be seen that the above approximation is valid for all
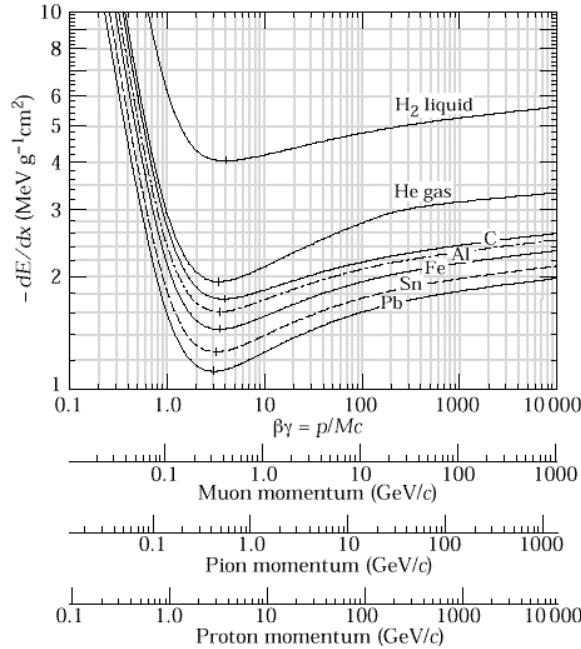
solids.

Figure 2: Energy loss rate in liquid hydrogen, gaseous helium, carbon, aluminium, tin and lead.

3.2   Energy Loss by Electrons

Above ≈1 GeV radiative processes dominate energy loss by electrons and photons. In the intense electric field of nuclei relativistic electrons radiate photons (*bremsstrahlung*) and photons are converted into electron-positron pairs (*pair creation*).

In dealing with electrons and photons at high energies striking blocks of material (e.g. calorimeters) it is convenient to measure the depth and radial extent of the resulting cascades in terms of *radiation length* (X_0) and *Moliére radius* (R_M).

Consider the process of bremsstrahlung. A free electron cannot radiate a photon. However a charged particle emits radiation when it is subjected to acceleration or deceleration. The acceleration/deceleration is greater the lighter the particle. The Feynman diagram for the bremsstrahlung process is shown in Figure 3. The cross section for the process comprises the coupling constant at the three vertices and the propagator term (α $1/m^2$)
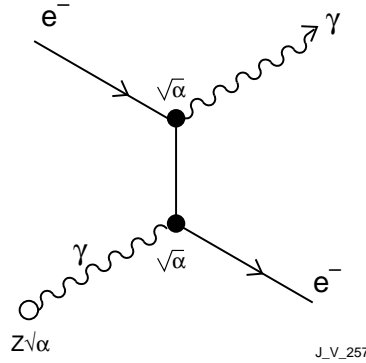
4

Figure 3: The Feynman diagram for bremstrahlung

$$\sigma \propto \frac{Z^2 \alpha^3}{m_e^2 c^4}$$

We are interested in $d\sigma/d\nu$ where ν is the energy of the emitted photon. We can make a guess for the expression using dimensional arguments:

$$\frac{d\sigma}{d\nu} \quad \alpha \quad \frac{Z^2 \alpha^3}{m_e^2 c^4} \frac{(\hbar c)^2}{\nu}$$

Turning this to energy loss per unit distance traversed by the electrons gives

$$-\frac{d\sigma}{dx}\Big|_{rad} = n \int_{\nu_{min}}^{\nu_{max}} \nu \frac{d\sigma}{d\nu} \, d\nu = n \frac{Z^2 \alpha^3 (\hbar c)^2}{m_e^2 c^4} \left(\nu_{max} - \nu_{min} \right)$$

where ν_{max} = kinetic energy of electron, $\nu_{min} \approx 0$ and n is no. of nuclei/unit volume. A numerical factor $[4 \ln(183/Z^{1/3})]$ has to be added describing the effect of the possible range of impact parameters of the electron. At large impact parameters the protons are shielded by atomic electrons. Hence

$$-\frac{dE}{dx}\Big|_{rad} = \left[4n \frac{Z^2 \alpha^3 (\hbar c)^2}{m_e^2 c^4} \ln \frac{183}{Z^{1/3}} \right] E \tag{2}$$

Since $-\frac{dE}{dx} \propto E \Rightarrow \frac{dE}{E} = - B \, dx \Rightarrow E = E_0 \, e^{-Bx}$

where B is a constant.

The *radiation length* is defined to be the distance over which the electron loses, on average, all but 1/e of its energy i.e. $X_0 = 1/B$ i.e

$$X_0 = \left[4n \frac{Z^2 \alpha^3 (\hbar c)^2}{m_e^2 c^4} \ln \frac{183}{Z^{1/3}} \right]^{-1}$$

and can be approximated as $X_0 \approx \dfrac{180A}{Z^2} \; g.cm^{-2}$

e.g. for Pb, Z = 82, n = $3.3.10^{28}$ nuclei/m^3, $X_0 \approx 5.3$ mm which is close to the PDG [9] value of 5.6 mm.
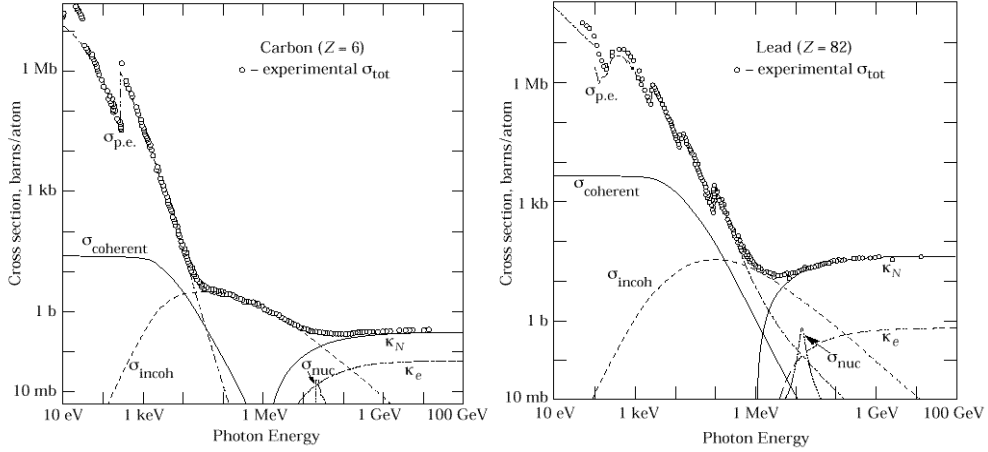

Figure 4: The photon total cross-sections as a function of energy in carbon and lead.

3.3 Energy Loss by Photons

Photons lose energy through photoelectric effect and Compton scattering at low energies and by pair production at relativistic energies. The cross-section for *photoelectric effect* is given by

$$\sigma_{pe} \approx Z^5 \alpha^4 \left(\frac{m_e c^2}{E_\gamma} \right)^n \quad n = \frac{7}{2} \; at \; E_\gamma << \; m_e c^2 \; and \; n \rightarrow 1 \; at \; E_\gamma >> \; m_e c^2$$

with a strong dependence on Z. The cross-section for *Compton scattering* has been calculated by Klein and Nishina :

$$\sigma_C \approx \frac{\ln E_\gamma}{E_\gamma} \; per \; electron \; and \; \sigma_C^{atom} = Z \; \sigma_C \; per \; atom$$

If the energy of the photon is $>> m_e c^2$ then the dominant energy loss mechanism is *pair production* and its probability can be deduced, as done in Equation (1) for bremstrahlung. It is given by:

$$\sigma_{pair} \approx \frac{7}{9} \frac{A}{N_A} \frac{1}{X_0}$$

6

The probability of a pair conversion in 1 X_0 is $e^{-7/9}$. Since the photon disappears on producing a pair a mean free path length can be defined as

$$L_{pair} = \frac{9}{7} X_0 \text{ independent of energy.}$$

The photon total cross-sections as a function of energy in carbon and lead are shown in Figure 4 [9] which shows the above mentioned dependences.

3.4 Critical Energy and Moliére Radius

The *critical energy*, ε, is defined to be the energy at which the energy loss due to ionisation (at its minimum i.e. at $\beta \approx 0.96$) and radiation are equal (over many trials) i.e.

$$\frac{(dE/dx)_{rad}}{(dE/dx)_{ion}} = \frac{Z\alpha}{\pi \, m_e c^2} E \, \beta^2 \frac{\ln 183/Z^{1/3}}{\ln\left[\frac{(2m_e c^2 \beta^2)}{I \, (1-\beta^2)}\right] - \beta^2} = 1$$

which simplifies to

$$\Rightarrow \quad \varepsilon \approx \frac{560}{Z} \quad (E \text{ in } MeV)$$

The Moliére radius gives the average lateral deflection of critical energy electrons after traversal of 1 X_0 and is parameterized as:

$$R_M = \frac{21_{MeV} X_0}{\varepsilon} \approx \frac{7A}{Z} \quad g.cm^{-2}$$

3.5 Hadronic Interactions

A high energy hadron striking an absorber interacts with nuclei resulting in multi-particle production consisting of secondary hadrons (e.g. $\pi^{\pm}$, π^0, K etc.). A simple model treats the nucleus, mass number A, as a black disc with radius R. Then

$$\sigma_{int} = \pi \, R^2 \propto A^{2/3} \quad where \, R \approx 1.2 \times A^{1/3} \, fm$$

$$\text{infact } \sigma_{inel} = \sigma_0 \, A^{0.7} \text{ where } \sigma_0 = 35 \, mb$$

The nuclear interaction length can be defined as $\quad \lambda_{int} = \frac{A}{N_A \sigma_{int}} \propto A^{1/3}$

In dealing with hadrons it is convenient to measure the depth and radial extent of the resulting cascades in terms of *interaction length* (λ_{int}).

The values of the above mentioned parameters for various materials are listed in Table. 1.

Table 1: Physical properties of some materials used in calorimeters.

	Z	ρ g.cm^{-3}	I/Z eV	$(1/\rho)dT/dx$ MeV/g.cm^{-3}	ε MeV	X_0 cm	λ_{int} cm
C	6	2.2	12.3	1.85	103	≈ 19	38.1
Al	13	2.7	12.3	1.63	47	8.9	39.4
Fe	26	7.87	10.7	1.49	24	1.76	16.8
Cu	29	8.96		1.40	≈ 20	1.43	15.1
W	74	19.3		1.14	≈ 8.1	0.35	9.6
Pb	82	11.35	10.0	1.14	6.9	0.56	17.1
U	92	18.7	9.56	1.10	6.2	0.32	10.5

4. THE ELECTROMAGNETIC CASCADE

4.1 Longitudinal Development

A high energy electron or photon incident on a thick absorber initiates a cascade of secondary electrons and photons via bremstrahlung and pair production as illustrated in Figure 5. With increasing depth the number of secondary particles increases while their mean energy decreases. The multiplication continues until the energies fall below the critical energy, ε. Ionization and excitation rather than generation of more shower particles dominate further dissipation of energy.
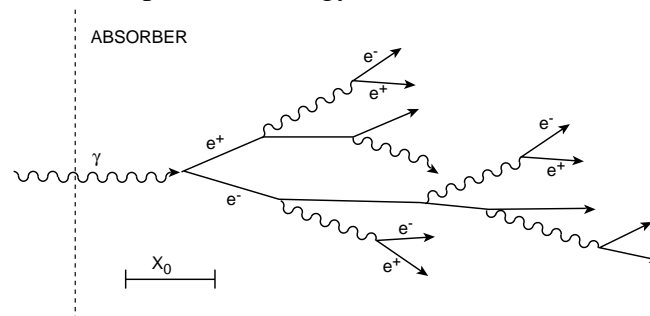
Figure 5: Schematic development of an electromagnetic shower.

Consider a simplified model of development of an electromagnetic shower initiated by an electron or a photon of an energy E. A universal description,

independent of material, can be obtained if the development is described in terms of scaled variables:

$$t = \frac{x}{X_0} \quad and \quad y = \frac{E}{\varepsilon}$$

Since in 1 X_0 an electron loses about 2/3rd of its energy and a high energy photon has a probability of 7/9 of pair conversion, we can naively take 1 X_0 as a generation length. In each generation the number of particles increases by a factor of 2. After t generations the energy and number of particles is

$$e(t) = \frac{E}{2^t} \quad and \quad n(t) = 2^t$$

respectively.

At shower maximum where $e \approx \varepsilon$, the no. of particles is

$$n(t_{max}) = \frac{E}{\varepsilon} = y \quad and \quad t_{max} = \ln \frac{E}{\varepsilon} = \ln y$$

Critical energy electrons do not travel far ($\leq 1X_0$). After the shower maximum the remaining energy of the cascade is carried forward by photons giving the typical exponential falloff of energy deposition caused by the attenuation of photons. Longitudinal development of 10 GeV showers in Al, Fe and Pb is shown in Figure 6 [3]. It can be noted that the shower maximum is deeper for higher Z materials because multiplication continues down to lower energies. The slower decay beyond the maximum is due to the lower energies at which electrons can still radiate. Both of the above effects are due to lower ε for higher Z materials.
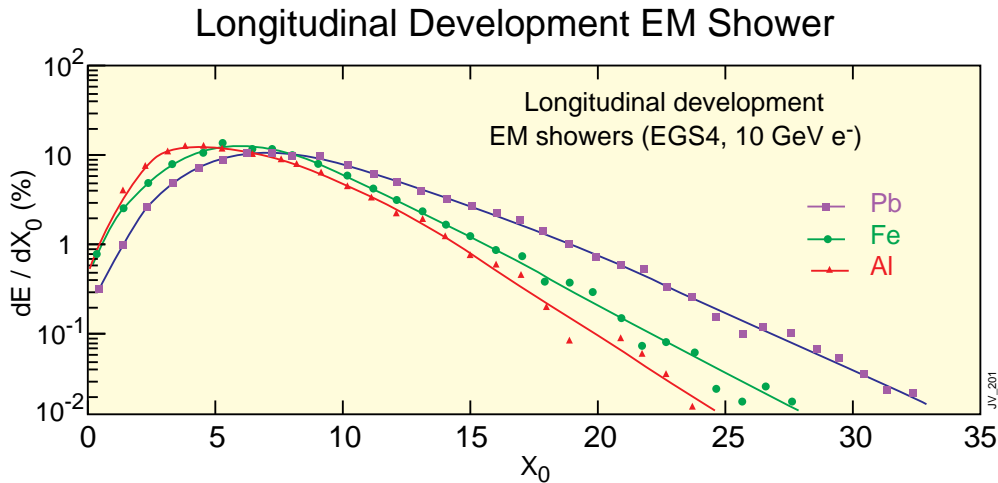

Figure 6: Simulation of longitudinal development of 10 GeV electron showers in Al, Fe and Pb.

The mean longitudinal profile of energy deposition is given by:

$$\frac{dE}{dt} = Eb\frac{(bt)^{a-1}e^{-bt}}{\Gamma(a)}$$

The maximum of the shower occurs at $t_{max} = (a-1)/b$. Fits to t_{max} give

$t_{max} = \ln y - 0.5$ for electron-induced cascades and

$t_{max} = \ln y + 0.5$ for photon-induced cascades.

The coefficient a can be found using t_{max} and assuming $b \approx 0.5$. The photon induced showers are longer since the energy deposition only starts after the first pair conversion has taken place. The m.f.p. length for pair conversion of a high energy photon is $X_\gamma = (9/7) X_0$.
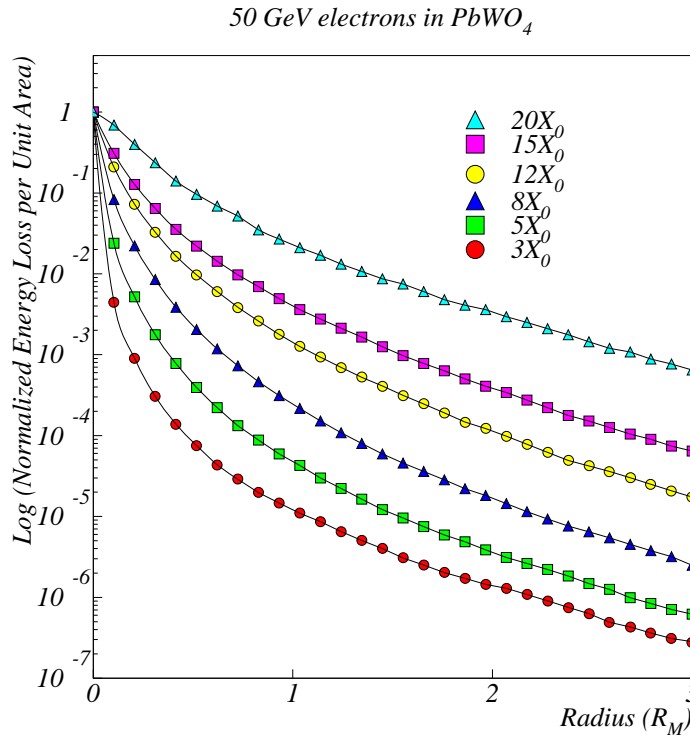

50 GeV electrons in PbWO$_4$

Figure 7: Lateral profile of energy deposition by 50 GeV electrons showers in PbWO$_4$ at various depths.

4.2 Lateral Development

The lateral spread of an e.m. shower is determined by multiple scattering of electrons away from the shower axis. Also responsible are low energy photons which deposit their energy a long way away from their point of emission, especially when emitted from electrons that already travel at large angles w.r.t. the shower axis. The e.m. shower begins, and persists, with a narrow core of high energy cascade particles, surrounded by a halo of soft

particles which scatter increasingly as the shower depth increases. This is shown in Figure 7 for 50 GeV electrons incident on lead tungstate [10]. In different materials the lateral extent of e.m. showers scales fairly accurately with the Moliére radius. An infinite cylinder with a radius of ≈ 1 R_M contains $\approx 90\%$ of the shower energy. For lead tungstate, and a depth of 26 X_0, the amount of energy contained in a cylinder of a given radius is shown in Figure 8. The fact that e.m. showers are very narrow at the start can be used to distinguish single photons from pizeros (see Section 7.2).
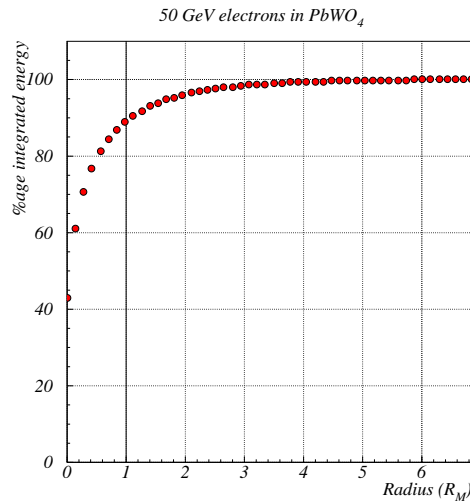

50 GeV electrons in PbWO$_4$

Figure 8: The percentage of energy contained in a cylinder of lead tungstate of different radii.

5   THE HADRONIC CASCADE

5.1   Longitudinal Development

A situation analagous to that for e.m. showers exists for hadronic showers. The interaction responsible for shower development is the strong interaction rather than electromagnetic. The interaction of the incoming hadron with absorber nuclei leads to multiparticle production. The secondary hadrons in turn interact with further nuclei leading to a growth in the number of particles in the cascade. Nuclei may breakup leading to spallation products. The cascade contains two distinct components namely the electromagnetic one (π^0s etc.) and the hadronic one ($\pi^\pm$, n, etc) one. This is illustrated in Figure 8.

The multiplication continues until pion production threshold is reached. The average number, *n*, of secondary hadrons produced in nuclear interactions is given by *n* α *ln E* and grows logarithmically. The secondaries are produced with a limited transverse momentum of the order of 300 MeV.
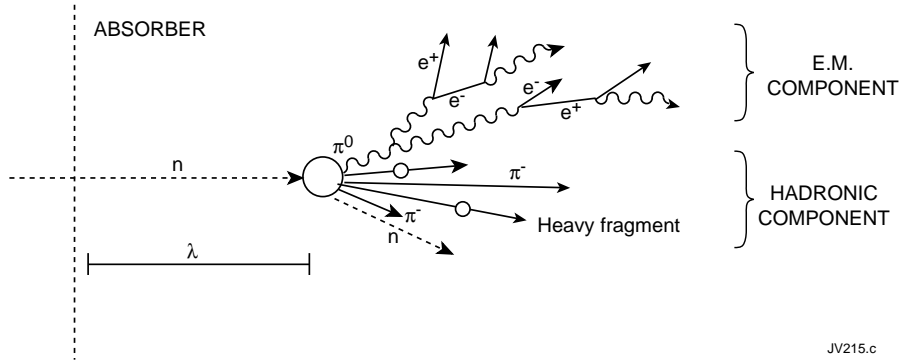
Fig. 9: Schematic of development of hadronic showers.

It is convenient to describe the average hadronic shower development using scaled variables

$$v = x/\lambda \quad and \quad E_{th} \approx 2m_\pi = 0.28 \, GeV$$

where λ is the nuclear interaction length and is the scale appropriate for longitudinal and lateral development of hadronic showers. The generation length can be taken to be λ. Note $\lambda \approx 35 \, A^{1/3}$ g.cm^{-2}. Furthermore, if it is assumed that for each generation <n> secondaries/primary are produced and that the cascade continues until no more pions can be produced then in generation v

$$e(v) = \frac{E}{\langle n \rangle^v}$$

$$e(v_{max}) = E_{th} \quad \therefore \quad E_{th} = \frac{E}{\langle n \rangle^{v_{max}}}$$

$$n^{v_{max}} = \frac{E}{E_{th}} \quad \Rightarrow \quad v_{max} = \ln(E/E_{th})/\ln\langle n \rangle$$

The number of independent particles in the hadronic cascades compared to electromagnetic ones is smaller by E_{th}/ε and hence the intrinsic energy resolution will be worse at least by a factor $\sqrt{(E_{th}/\varepsilon)} \approx 6$. The average longitudinal energy deposition profiles are characterised by a sharp peak near the first interaction point (from π^0s) followed by a exponential fall-off with scale λ. This is illustrated in Fig. 9. The maximum occurs at $v_{max} \approx 0.2 \, lnE + 0.7$ (E in GeV).

It can be seen that over 9λ are required to contain the energy of high energy hadrons. A parameterisation for the depth required for almost full containment (95%) is given by $L_{0.95}(\lambda) \approx t_{max} + 2\lambda_{att}$ where $\lambda_{att} \approx \lambda \, E^{0.13}$.
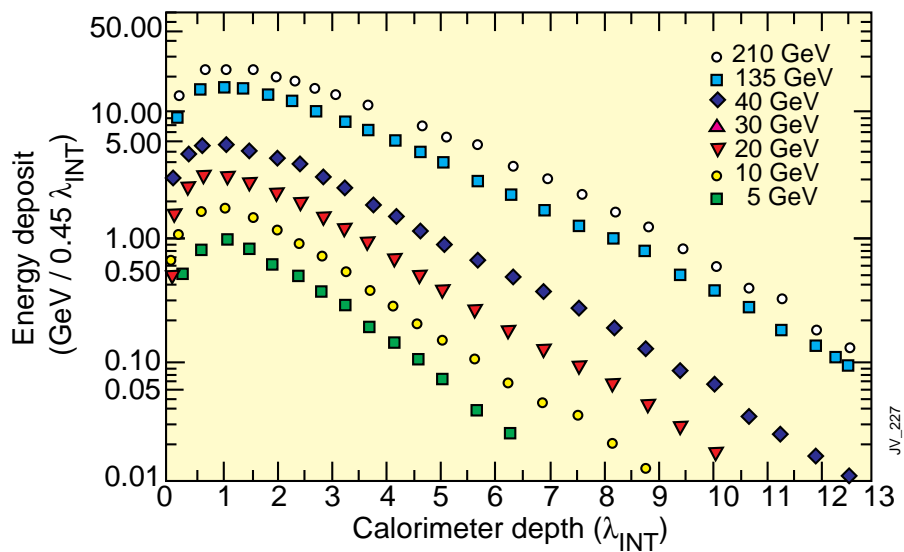
12

Fig. 10: longitudinal profile of energy deposition for pion showers of different energies.
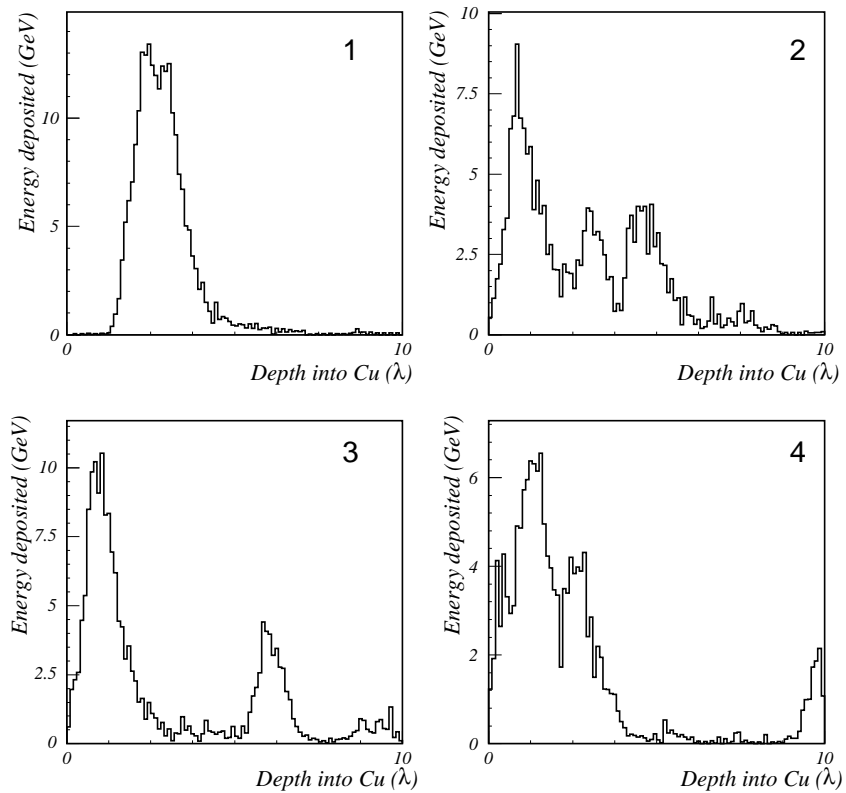
270 GeV Incident Pions in Copper

Figure 11: A simulation of the development of four representative pion showers in a block of copper.

13

There is a considerable variation from one hadronic shower to another as illustrated in Fig. 11 [10]. The peaks arise from energy deposited locally by π^0s produced in the interactions of charged hadrons. These interactions take place at differing depths from shower to shower. The energy carried by π^0s also varies considerably from shower to shower.

5.2   Lateral Development

The secondary hadrons are produced typically with $<p_t> \approx 300$ MeV. This is comparable to the energy lost in 1λ in most materials. At shower maximum, where the mean energy of the particles is $E_{th} \approx 280$ MeV, the radial extent will have a characteristic scale of $R_\pi \approx \lambda$. High energy hadronic showers show a pronounced core, caused by the π^0 component with a characteristic transverse scale of R_M, surrounded by an exponentially decreasing halo with scale λ. This is illustrated in Figure 12 for a lead/scintillating fibre calorimeter [12].

150 GeV Pion Shower Profile

$$r\,f(r) = B_1 \exp(-r/\lambda 1) + B_2 \exp(-r^2/\lambda)$$

$\lambda_1 = 14.3$ cm
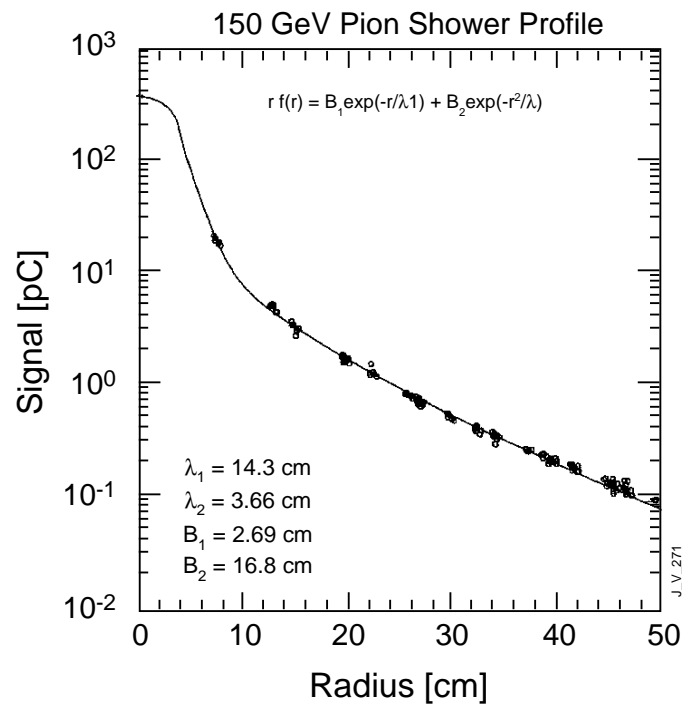$\lambda_2 = 3.66$ cm
$B_1 = 2.69$ cm
$B_2 = 16.8$ cm

Figure 11: The lateral profile of energy deposition of pion showers.

14

6. THE ENERGY RESOLUTION

The energy resolution of calorimeters is usually parameterised as :

$$\frac{\sigma}{E} \;=\; \frac{a}{\sqrt{E}} \;\otimes\; \frac{b}{E} \;\otimes\; c$$

where the r.h.s. is assumed to be the square root of the quadratic sum of the three terms.

The first term, with coefficient a, is the *stochastic or sampling* term and accounts for the statistical fluctuation in the number of primary and independent signal generating processes, or any further process that limits this number. An example of the latter is the conversion of light into photo-electrons by a photo-device.

The second term, with coefficient b, is the *noise* term and includes:
- the energy equivalent of the electronics noise and
- the fluctuation in energy carried by particles, other than the one(s) of interest, entering the measurement area. This is usually labeled pileup.

The last term, with coefficient c, is the *constant* term and accounts for:
- imperfect quality of construction of the calorimeter
- non-uniformity of signal generation and/or collection
- cell-to-cell inter-calibration error
- the fluctuation in the amount of energy leakage from the front, the rear and the sides of the volume used for the measurement of energy,
- the fluctuation in the amount of energy deposited in dead areas in front or inside the calorimeter,
- the contribution from the fluctuation in the e.m. component in hadronic showers.

The tolerable size of the three terms depends on the energy range involved in the experiment. The above parametrisation allows the identification of the causes of resolution degradation. The quadratic summation implies that the three types of contributions are independent which may not always be the case.

6.1   Intrinsic Electromagnetic Energy Resolution

It is instructive to look at homogeneous calorimeters in which all the energy is deposited in the active medium. If the shower is fully contained then the intrinsic energy resolution is determined by the fluctuation in the number, n,

of ions or photons produced. If W is the mean energy required to produce an electron-ion pair (or a photon) then $n = E/W$, and

$$\frac{\sigma}{E} = \frac{\sqrt{n}}{n} = \sqrt{\frac{W}{E}}$$

However the fluctuation is smaller as the total energy deposited (= incident energy) does not fluctuate. The improvement in resolution is characterised by the Fano factor, F, as

$$\frac{\sigma}{E} = \sqrt{F} \times \sqrt{\frac{W}{E}} = \sqrt{\frac{FW}{E}}$$

F is dependent on the nature of processes that lead to energy transfer in the detector including ones that do not lead to ionisation e.g. phonon excitations.

Consider calorimeters used for the spectroscopy of low energy ($\approx$MeV). gamma rays. The two commonly used detectors are inorganic scintillators (e.g. NaI) and semiconductor detectors (e.g. Ge). The energy resolution of the Ge detector is superior and is measured to be $\sigma \approx 180$ eV for photons carrying 100 keV. The above formula gives $\sigma = \sqrt{(FEW)} \approx 195$ eV where $F_{Ge}=0.13$ and W=2.96 eV. It should be noted that without the Fano factor $\sigma \approx 540$ eV!

Another illustration employs noble liquids for the energy measurement. In principle a precision similar to that for Ge should be possible. However, the [207]Bi electron conversion line at 976 keV in liquid argon yields $\sigma \approx 11$ keV whereas the above formula would give

$$\sigma = \sqrt{(FEW)} = \sqrt{(0.11 x 23.7 x 976 x 10^3)} \approx 1.6 \; keV.$$

An additional source of fluctuation is in the amount of energy going into mechanisms other than one being used for measurement e.g. scintillation when ionisation charge is collected. Not all the created electron-ion pairs contribute to the collected charge. In the absence of electric field about half of the pairs recombine and give scintillation light through molecular de-excitation. If $n = n_{ion} + n_{scint}$ and only charge is collected then

$$\sigma_{ion} = \sqrt{n \; \frac{n_{ion}}{n} \; \frac{n_{scint}}{n}} = \sqrt{\frac{n_{ion}(n - n_{ion})}{n}}$$

Measuring both light and charge can improve the resolution e.g. if $n_{ion}/n = 0.9$ then the resolution improves by a factor 3 w.r.t. the Poisson expectation ($\sqrt{n_{ion}}$). The improvement is illustrated in Figure 13 [13]
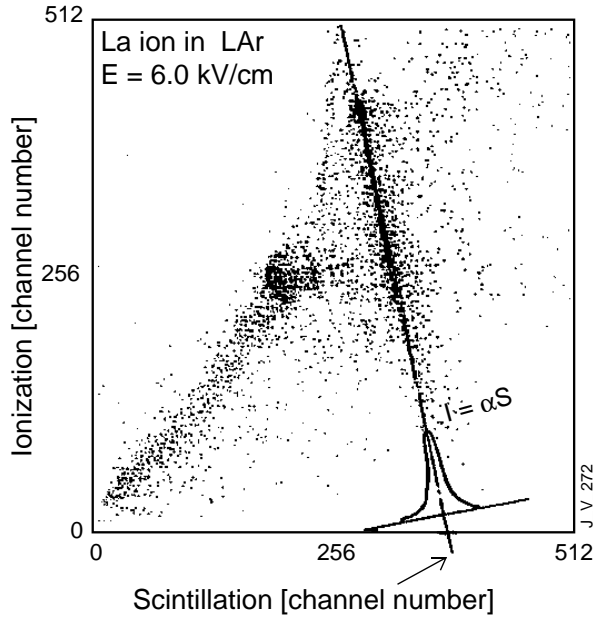
Figure 13: The anti-correlation between the ionization signal and the scintillation light in liquid argon.

Other phenomena may limit the number of signal generating events. Lead glass shower detectors are based on the detection of Cerenkov light, produced by the electrons and positrons with kinetic energies greater than ~ 0.7 MeV. This means that at most 1000 / 0.7 ~ 1400 independent particles, per GeV of deposited energy, produce Cerenkov light. The resolution is then dominated by the fluctuation in this number and thus cannot be better than $\sigma/E = \sigma_n \geq 3\% / \sqrt{E}$. This is further limited by photo-electron statistics as only about 1000 photo-electrons are generated when using photomultipliers to detect the scintillation light. This leads to an additional loss of resolution given by $\sigma_{pe} \approx 3\% / \sqrt{E}$.

6.2   Electromagnetic Energy Resolution – Constant Term

6.2.1   *Longitudinal Non-Uniformity*

Longitudinal non-uniformity of signal generation and/or collection either intrinsically or through radiation damage, when folded with the shower-to-shower fluctuation in the longitudinal profile (at a fixed energy) leads to a loss of energy resolution. Since the fluctuation is essentially independent of energy a contribution to the constant term arises. The fluctuation of the shower maximum is plotted in Figure 14 [14] for 50 GeV electrons giving $\sigma \approx 1 X_0$.
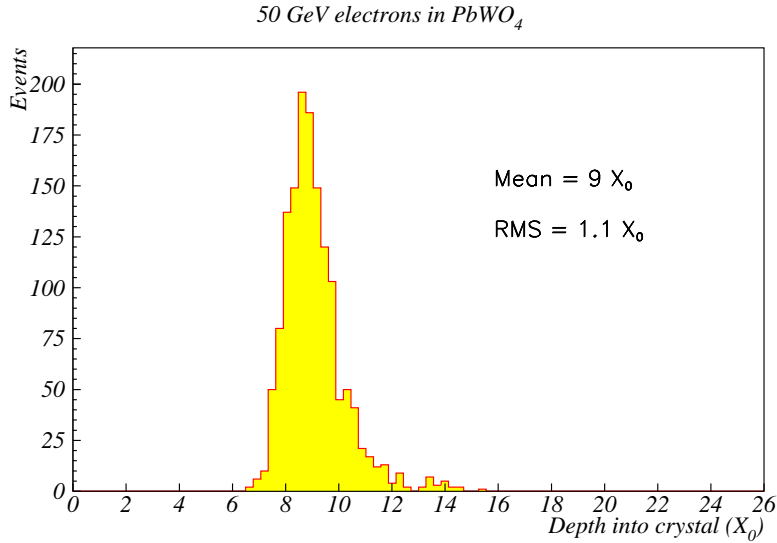
17

Figure 14: The position of the shower maximum for 50 GeV electrons in PbWO$_4$.

The ideal light collection efficiency as a function of distance from the photo-device end for PbWO$_4$ crystals for CMS is shown in Figure 15a [14]. The collection efficiency in the region of the shower maximum (5-10 X$_0$) should be constant with a slight increase at the rear of the crystals (photo-sensor end) to compensate for the energy leakage in showers developing late. The measured correlation between the slope of the light collection efficiency function in the region of shower maximum and the induced constant term is shown in Figure 15b.

6.2.2   Cell-to-cell Intercalibration Error

Electromagnetic showers are narrow and usually the central cell, or at most, the central 4 cells contain most of the energy of the shower. Since the lateral shower shape is nearly independent of energy, any effect due to imperfect cell-to-cell inter-calibration will end up in the constant term. If the reconstructed energy is E = Σ g$_i$.E$_i$ and if the r.m.s. error on g$_i$ is δ then the constant term will range from δ /$\sqrt{N}$ where N is the number of cells with significant energy i.e. from δ /2 and δ /4. This implies that the cell-to-cell intercailbration error should be substantially better than the desired constant term.

At the LHC the rate of isolated electrons from the electronic decays of W and Z bosons is large: 45 Hz at L=10^{34} cm^{-2}s^{-1} with p$_T$ > 20 GeV in the region |η| < 1.5. These electrons will be used to establish the calibration. In a study by CMS [8, ECAL TDR] stringent cuts on isolation parameters are made to select electrons that have lost only a small amount of energy due to bremsstrahlung. The isolation condition requires that the energy contained in a matrix of 3x3 crystals, centred on the electron impact, is more than 92%

of the energy contained in a larger matrix of 7x11 crystals. The energy, E, is then compared with the electron momentum, p, measured in the inner tracker. As an example the resolution on the parameter E/p is found to be $\sigma_{E/p} \approx 1.5\%$ at $\eta = 0.9$ with a reconstruction efficiency of about 45%. The statistical precision on the calibration coefficient improves as $\sigma_{E/p}/\sqrt{N_e}$ where N_e is the number of usable electrons. Hence about 25 good electrons per crystal will be sufficient to achieve the design goal of a calibration (and inter-calibration) uncertainty of 0.3%.
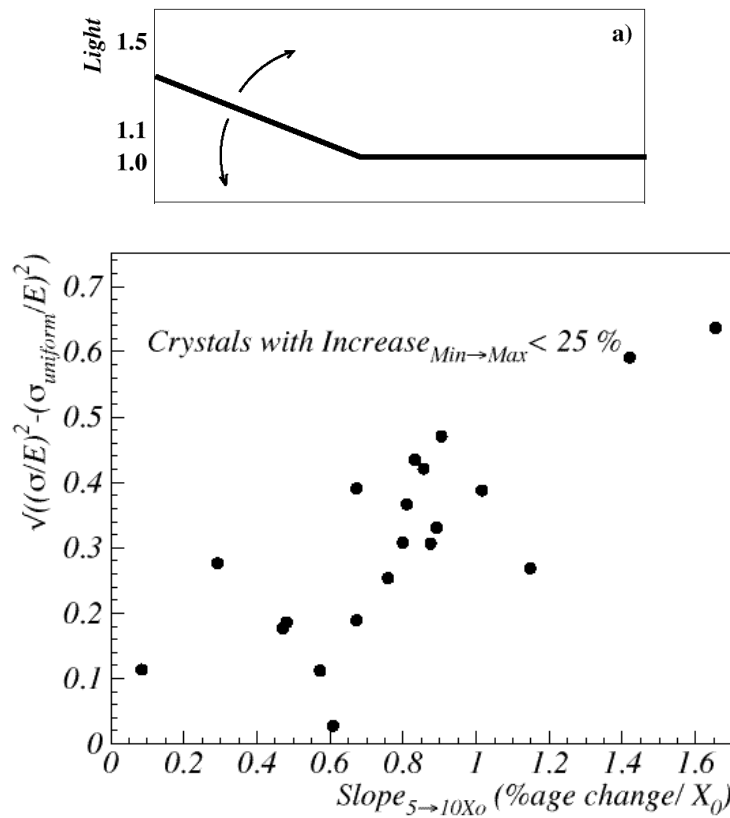

Figure 15: a) The ideal light collection efficiency as a function of distance from photosensor end for $25X_0$ deep crystals, b) The measured correlation between the slope in the region of shower maximum and the induced constant term.

The calibration of the hadronic calorimeter can be established using selected events containing high p_T photons or Z bosons balanced by a single jet. It may also be possible to use single pions from $\tau^\pm \to \pi^\pm \nu_\tau$ decays. The momentum of the charged pion, measured in the tracker, can be comparewd with the energy measured in the calorimeter.
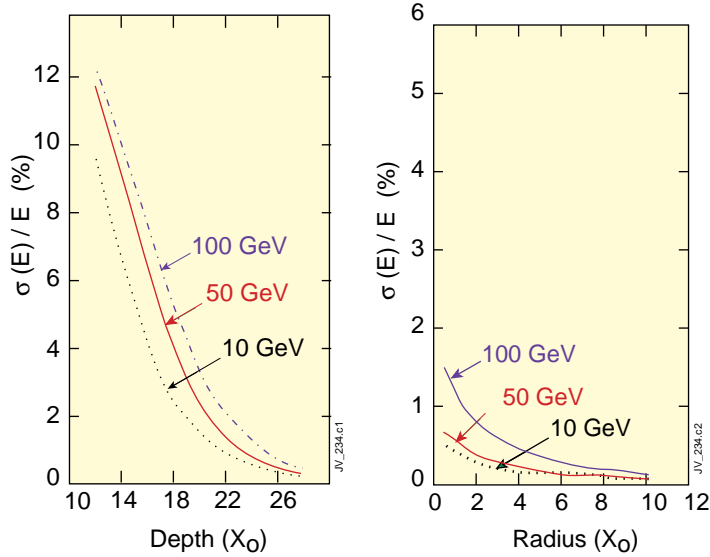
Figure 16: The effect of a) longitudinal and b) lateral energy leakage on energy resolution
of LXe calorimeter. Note $R_M(LXe) \approx 1.5\ X_0$.

6.2.3   Energy Leakage

Energy leakage, from the calorimeter volume used for the energy
measurement, leads to a degradation of energy resolution. Figure 16
illustrates the degradation due to longitudinal and lateral energy leakage for
a homogeneous LXe calorimeter. Longitudinal leakage clearly has more
serious consequences. At a fixed energy the profile of the longitudinal
energy deposition differs from one shower to another. Showers developing
late lead to a larger energy leakage from the rear of a finite depth
calorimeter. The fraction of the incident energy leaking out, and the
fluctuation on it, increases with energy since the depth at which the shower
maximum occurs increases with energy, albeit logarithmically. The r.m.s.
deviation, as a fraction of the mean deposited energy, versus the fractional
longitudinal energy leakage (f) is plotted in Figure 16. For a calorimeter
with a fixed depth

$$\frac{\sigma_{rms}}{\left\langle E_{dep} \right\rangle} \;=\; \frac{f}{2} \quad for \;\; f \;<\; 20\%$$

The loss of energy resolution due to the lateral energy leakage is smaller
since the lateral profile of energy deposition differs much less from one
shower to another. The energy dependence of the fluctuation is also weak as
the lateral shower shape is almost independent of energy especially at high
energies.

6.3 Energy Resolution of Sampling Electromagnetic Calorimeters

When the very best energy resolution is not required, sampling calorimeters are employed. The shower energy is measured in active layers, often of low Z, sandwiched in between passive absorber layers of high Z materials. Only a fraction of the shower energy is dissipated in the active medium and the energy resolution is dominated by the fluctuation in this fraction. If the energy loss in an active layer is much smaller than that in the absorber layer then the number of independent charged particles crossing an active layer can be approximated by $n=E/\Delta E_{abs}$ where ΔE_{abs} is the energy lost by a minimum ionizing particle (m.i.p.) in the absorber layer.

Now $\Delta E_{abs} = t_{abs} \times (dE/dx)$ where t_{ab} is measured in units of X_0. Hence

$$\frac{\sigma}{E} = \frac{\sqrt{n}}{n} \propto \frac{\sqrt{t_{abs}}}{\sqrt{E}}$$

For a fixed thickness of an active layer the energy resolution improves with decreasing absorber thickness. The above formula is not valid if the crossings between consecutive active layers are correlated, i.e. when t_{abs} is small. A generally valid formula is:

$$\frac{\sigma_s}{E} = \frac{5\%}{\sqrt{E}} \left(1 - f_{samp}\right) \Delta E_{cell}^{0.5\left(1-f_{samp}\right)}$$

where ΔE_{cell} is the energy deposited in a unit sampling cell i.e. 1 active and 1 absorber layer. f_{samp} is labeled the *sampling fraction* and is the fraction of the total energy that is deposited in the active medium.

As $f_{samp} \rightarrow 1$, σ_s = 'a' $\rightarrow 0$ (usually a $\neq 0$ due to imperfections in calorimeter systems) and as $f_{samp} \rightarrow 0$, σ_s α $\sqrt{\Delta E_{cell}}$ α $\sqrt{\Delta E_{abs}}$

The sampling fraction can be calculated as follows. If d is the thickness of active layer then

$$f_{samp} = 0.6 f_{mip} = 0.6 \frac{d \left(\frac{dE}{dx}\right)_{act}}{\left[d \left(\frac{dE}{dx}\right)_{act} + t_{abs} \left(\frac{dE}{dx}\right)_{abs}\right]}$$

For a sampling calorimeter with 1 cm Pb and 1 cm scintillator plates $f_{mip} \approx 2/(12.75+2) \approx 13.5\%$. The fractional energy resolution as a function of $\sqrt{(d/f_{samp})}$ is shown in Figure 17 [15]. Clearly the energy resolution of gas calorimeters will be poor as the sampling fraction tends to be very low.
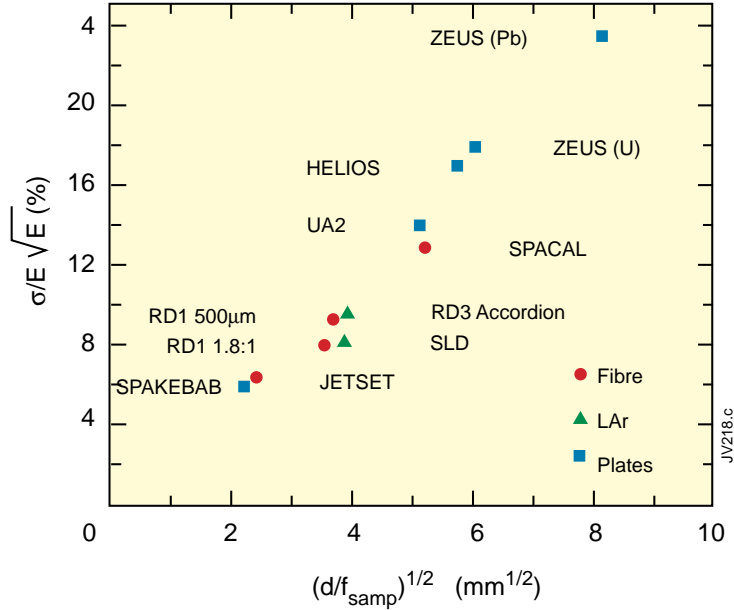
Figure 17: The fractional energy resolution of some calorimeters as a function of $\sqrt{(d/f_{samp})}$

6.4   Energy Resolution of Hadronic Calorimeters

Hadronic calorimeters, because of the large depth required ($\approx 10\lambda$), are by necessity sampling calorimeters. The response of a sampling electromagnetic calorimeter can be expressed as

$$E_{vis} \ = \ e \ E$$

where E, E_{vis} are incident and visible energies respectively and $e = f_{samp}$, the lectromagnetic sampling fraction. Similarly the response of a hadronic sampling calorimeter is

$$E_{vis} \ = \ e \ E_{em} \ + \ \pi \ E_{ch} \ + \ n \ E_{n} \ + \ N \ E_{nucl}$$

where E_{em}, E_{ch}, E_{n}, E_{nucl} are respectively the energy deposited by electromagnetic component, charged hadrons, low energy neutrons and energy lost in breaking up nuclei. Each component has its own sampling fraction. N is normally very small but E_{nucl} can be large e.g. it is $\approx$ 40% in Pb calorimeters. Hence the ratio of the response to electromagnetic and hadronic showers i.e. e/h is usually > 1 and the hadronic calorimeter is said to be *non-compensating*.

In hadronic calorimeters the fluctuation in the visible energy has two sources :
• sampling fluctuations as in the e.m. case which can be reduced by finer sampling and

- intrinsic fluctuation in the shower components (δE_{em}, δE_{ch} etc.) from shower to shower as seen in Figure 11.

Therefore the stochastic term is given by

$$a_h = \sigma_{samp} \oplus \sigma_{intr}$$

$$\sigma_{samp} = \frac{a}{\sqrt{E}} \quad where \quad a \approx 10\% \sqrt{\Delta E_{cell}}$$

$$\sigma_{intr} = \frac{a_{intr}}{\sqrt{E}} + c$$

where c is the constant term which depends on e/h and vanishes for a compensating calorimeter.

6.4.1   The Neutral Component in Hadronic Cascade and the Role of e/h

The hadronic showers have an electromagnetic component (F_0) which is determined essentially by the first interaction. There is a considerable event-to-event fluctuation in F_0. On average the neutral e.m. energy per interaction is f_0=1/3 as roughly one-third of the mesons produced in hadronic interations will be neutral [e.g. $(\pi^0/(\pi^+ + \pi^- + \pi^0)) \approx 1/3$]. If sufficiently energetic the 2nd generation $\pi^\pm$ may also produce π^0s. The value of F_0 after n generations can be estimated as follows. For

n=1 $F_0 \rightarrow f_0$
n=2 $F_0 \rightarrow f_0 + f_0 (1 - f_0)$
n=3 $F_0 \rightarrow f_0 + f_0 (1 - f_0) + f_0 (1 - f_0)^2$
………
$F_0 = [1 - (1-f_0)^\nu]$

This leads to $F_0 \rightarrow f_0$ at low energies and $F_0 \rightarrow 1$ at very high energies as n is large. This can be seen in Figure 18 [16] which shows a simulation of pions of 20 GeV and 200 GeV incident on lead. A large event-to-event fluctuation in the neutral fraction is evident. The increase in F_0 with energy is due to the fact that neutral pions, developing as e.m. showers, do not produce any hadronic interactions.

It usually turns out that the response to electrons and photons i.e. the e.m. component (labeled *e*) differs from that due to charged hadrons i.e. the non-e.m. component (labeled *h*). If E is the incident energy the response to electrons (E_e) and charged pions (E_π) can be written as :

$E_e = e\,E, \qquad E_\pi = [\,e\,F_0 + h\,(1 - F_0)\,]\,E \quad$ leading to

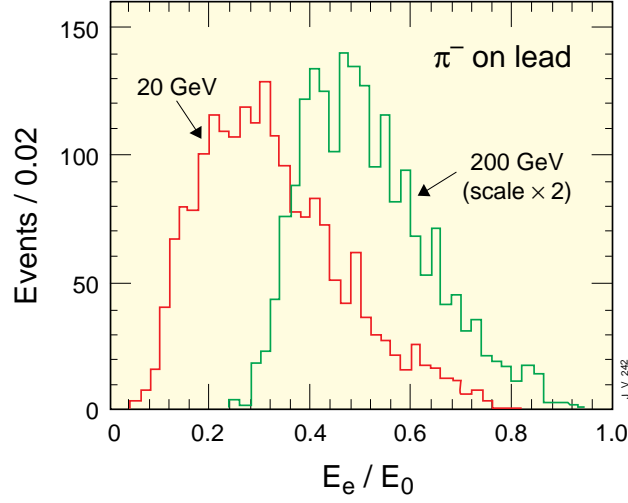$$\frac{e}{\pi} = \frac{(e/h)}{\left[(e/h)F_0 + (1 - F_0)\right]}$$

Figure 18: Distribution of e.m. energy fraction for charged pions incident on lead.

If e/h = 1 the calorimeter is said to be compensating.
Consider $dE_\pi = [(e - h) dF_0] E$. Then

$$\frac{dE}{E} = \frac{dF_0 \left|(e/h) - 1\right|}{\left[(e/h)F_0 + (1 - F_0)\right]}$$

Hence the fractional error depends on e/h, F_0 and dF_0. If e/h=1 then there is no contribution due to the fluctuation dF_0. For example:

$$\frac{dF_0}{F_0} = \frac{df_0}{f_0} \sim \frac{1}{\sqrt{f_0\langle n\rangle}}$$

i.e. for a 200 GeV hadron, $\langle n\rangle \approx 9$, $dF_0 \approx 0.6 \Rightarrow (dE/E)_{comp} \approx 3.5\%$.

$$\left.\frac{dE}{E}\right|_{comp} \sim \frac{1}{\sqrt{\ln E}} \quad and \quad \to 0 \quad as \quad E \to \infty \quad since \quad \langle n\rangle \propto \ln E$$

This aspect is illustrated by calorimeters using quartz fibres as active media. Charged particles traversing the fibres generate Cerenkov light which is guided to photomultipliers by the fibres themselves. Such a technique is employed by CMS for calorimetry in the very forward region ($3 < |\eta| < 5$) [8]. The aim is to measure the energies of, and tag, high energy jets from the WW fusion process. The signal in the calorimeter arises predominantly from the electromagnetic component as charged hadrons have a very high Cerenkov threshold when compared to that of electrons. Hence e/h is very large and the energy resolution at high energies will be dominated by the fluctuation in F_0. The resolution should improve as $1/\ln E$ rather than as $1/\sqrt{E}$. Figure 19 shows the measured energy resolution of the CMS

copper/quartz fibre calorimeter. Also shown is the resolution after subtraction of the contribution from photostatistics. It should be noted that the photostaistics contribution is sizeable as only about 1 photoelectron per GeV is generated.
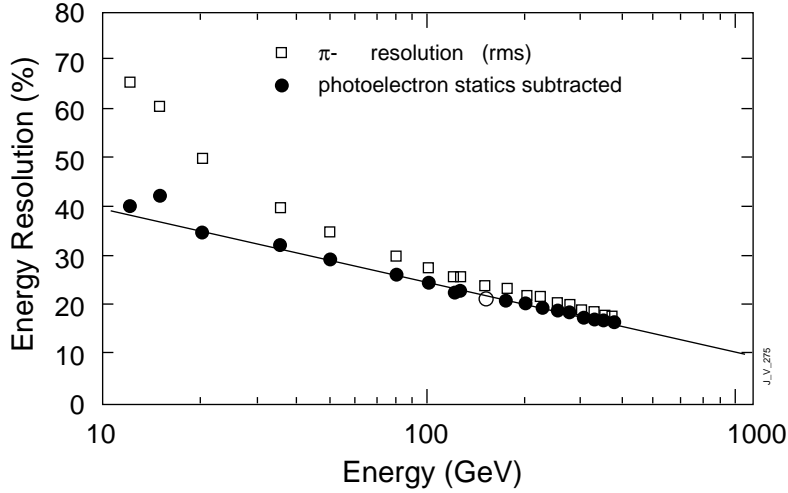

Figure 19: The measured pion energy resolution of a copper/quartz fibres calorimeter.

If |e/h| ≥ 10% the performance of the calorimeter is compromised because of the fluctuation in the π^0 content of the cascades. This leads to:
• a non-Gaussian measured energy distribution for mono-energetic hadrons,
• an e/π ratio that is different from unity and that varies with energy,
• a non-linear response in energy to hadrons,
• an additional contribution to the relative energy resolution (σ/E),
• a σ/e that does not improve as 1/√E.
These effects have been observed and are illustrated in Figure 20 [3].
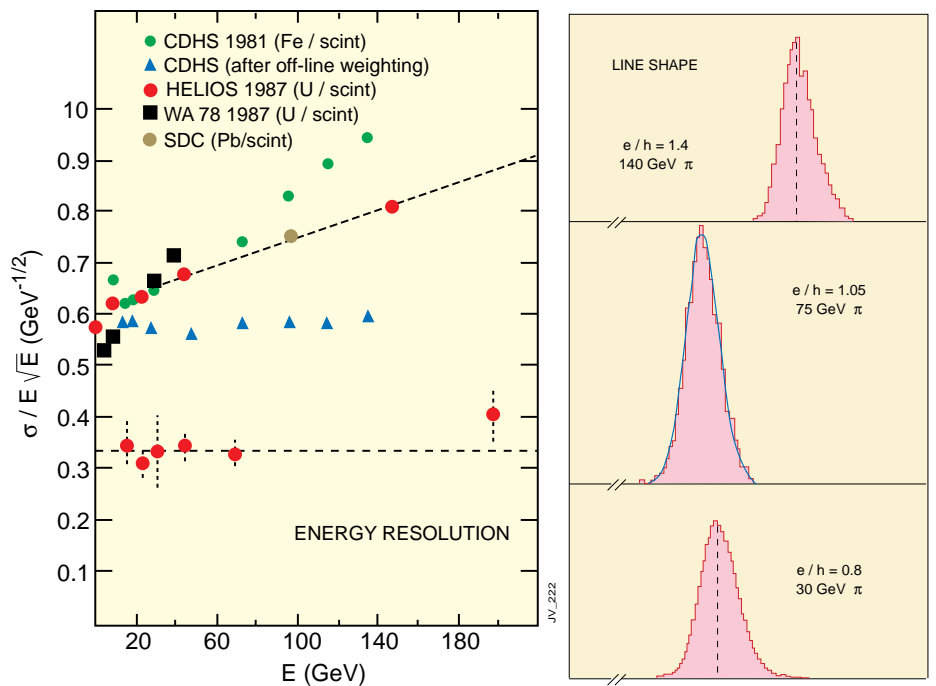
6.4.2   Compensation

The degree of (non-) compensation is expressed by the energy independent ratio *e/h*.. Th *e/h* ratio cannot be measured directly but can be inferred from the energy dependent e/π signal ratios. Two relations between the signal ratio e/π(E) and e/h by Groom [16] and Wigmans [17] are :
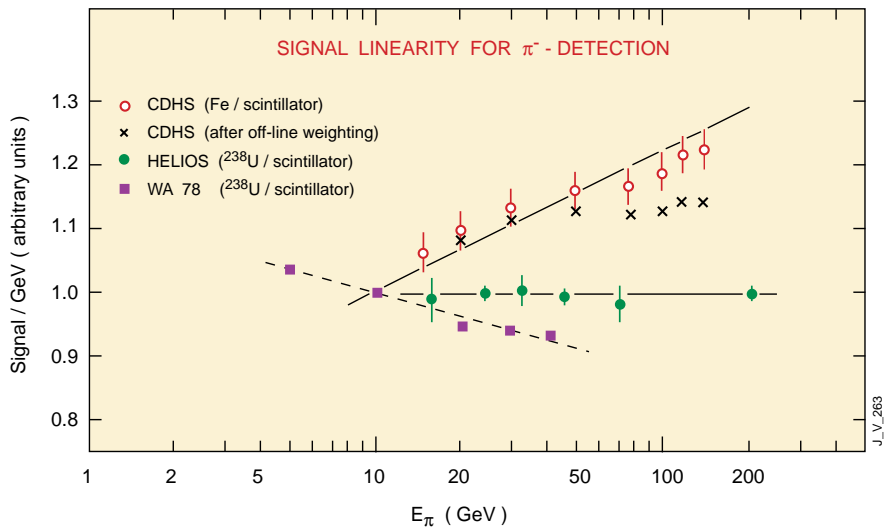
$$\frac{e}{\pi} = \frac{e/h}{1 + (e/h - 1)F_0}$$

$$F_0 = 1 - (E/0.76)^{-0.13} \quad D.\ Groom$$

$$or \quad F_0 = 0.11 \ \ln E \quad \quad R.\ Wigmans$$

25

a)

b)

c)

Figure 20: Experimental observation of the consequences of e/h≠1 [3]: a) the energy resolution: (σ/E).√E is plotted to show deviations from scaling for non-compensating devices, b) line-shape for monoenergetic pions is only Gaussian for the compensating calorimeter, c) the signal/GeV plotted as a function of pion energy, showing signal non-linearity for non-compensating calorimeters.

It is instructive to see how the energy is dissipated by a hadron in a Pb absorber. The breakdown of the dissipated energy is as follows:

    42% in breaking up nuclei and not rendered measurable (invisible)
    43% by charged particles
    12% by neutrons with kinetic energy ~ 1 MeV
     3% by photons with an energy ~ 1 MeV.

The sizeable amount of invisible energy loss means that hadronic calorimeters tend to be under-compensating (e/h > 1).

 Compensation can be achieved in three ways;
    boost the non-e.m. response using depleted uranium,
    suppress e.m. response
    boost the detectable response to low energy neutrons.

The ZEUS Collaboration[18] have found that achieving compensation for U/scintillator and Pb/scintillator calorimeters requires absorber/scintillator plate thickness ratios given by 1:1 and 4:1 respectively. They also used the technique of interleaved calorimeters to determine the intrinsic energy resolution of U and Pb calorimeters. This is accomplished by reading out odd and even scintillator layers separately. The results are as follows:

hadrons	Pb	$\sigma_{samp} = 41.2 \pm 0.9\%/\sqrt{E}$	$\sigma_{intr} = 13.4 \pm 4.7\%/\sqrt{E}$
	U	$\sigma_{samp} = 31.1 \pm 0.9\%/\sqrt{E}$	$\sigma_{intr} = 20.4 \pm 2.4\%/\sqrt{E}$
electrons	Pb	$\sigma_{samp} = 23.5 \pm 0.5\%/\sqrt{E}$	$\sigma_{intr} = 0.3 \pm 5.1\%/\sqrt{E}$
	U	$\sigma_{samp} = 16.5 \pm 0.5\%/\sqrt{E}$	$\sigma_{intr} = 2.2 \pm 4.8\%/\sqrt{E}$

The intrinsic fluctuations in a compensating Pb calorimeter are smaller than those for a U one. However the sampling has to be much coarser for Pb calorimeter leading to a much poorer e.m. energy resolution. ZEUS therefore chose U as the absorber material. It can also be seen that for compensating Pb and U calorimeters the energy resolution is dominated by sampling fluctuations and is given by

$$\sigma_{samp} = \frac{11.5\% \sqrt{\Delta E_{cell}(MeV)}}{\sqrt{E(GeV)}}$$

The sampling fluctuations for hadrons are larger than those for e.m. showers by a factor of 2. From the above it is evident that very good e.m. energy resolution is incompatible with e/h=1.

6.5   Jet Energy Resolution

Hadronic calorimeters are primarily used to measure the energies of jets and hence the quantities that characterize their are:
• jet energy resolution and energy linearity,

• missing transverse energy resolution.

The jet energy resolution is limited by effects from
• algorithms used to define jets (energy is dependent on cone radius, lateral segmentation of cells etc.),
• the fluctuation in the particle content of jets due to differing fragmentation from one jet to another,
• the fluctuation in the underlying event,
• the fluctuation in energy pileup in high luminosity hadron colliders
• magnetic field.

In experiments on e+e- machines the jet energy resolution can be improved as the centre of mass energy can be used to constrain the energies of jets if the jet directions are measured relatively precisely.

6.5.1   Jet Energy Resolution

Jet energy resolution can be deduced using single particle resolution in the limit that either stochastic or constant terms dominate. Consider two cases: one in which a single particle with energy E and the second in which a jet of particles, each carrying energy $k_i = z_i E$ where $\Sigma z_i = 1$, is incident on the calorimeter. Assume first that the stochastic terms dominate. Since

$$\frac{\sigma(E)}{E} \; = \; \frac{a}{\sqrt{E}} \; \oplus \; c$$

$$\sum_i z_i \; = \; 1, \quad \sum_i k_i \; = \; E \qquad \frac{dk_i}{k_i} \; = \; \frac{a}{\sqrt{k_i}} \; \oplus \; c$$

$$dk_i \; = \; a \; \sqrt{k_i}$$

$$dE_J \; = \; \sqrt{\sum_i (dk_i)^2} \; = \; \sqrt{\sum_i a^2 k_i} \; = \; a\sqrt{E}$$

$$\therefore \; \frac{dE}{E} \; = \; \frac{a}{\sqrt{E}}$$

Therefore an ensemble of particles act, with respect to errors, as a single particle. In the high energy regime where the constant term dominates

$$dE_J \; \approx \; \sqrt{(cz_i E)^2} \; = \; cE\sqrt{z_i^2}$$

Assuming that there is a leading particle, *l*, with energy fraction z*l*, then

$$\frac{dE_J}{E} \approx c \ E \ z_l$$

For fragmentation function $zD(z) = (1-z)^2$ $\langle z_l \rangle \approx 0.23$ implying that the constant term is reduced. For a calorimeter with a = 0.3 and c = 0.05, in which a 1 TeV jet fragments into 4 hadrons of equal energy, the error on the energy decreases form 50 GeV to 25 GeV.

6.5.2   Di-Jet Mass Resolution v/s Cone Size

One figure of merit of a hadron calorimeter is di-jet mass resolution. For the purposes of measuring the jet energy resolution low p_t di-jets (50 <p_t<60 GeV), high p_t di-jets (500 <p_t<600 GeV) and high mass di-jets (3 < $m_{Z'}$<4 TeV) at the LHC can be used [19]. The mass resolution for the three categories v/s cone size, ΔR, where $\Delta R = \sqrt{(\Delta\eta^2+\Delta\phi^2)}$ in pseudorapidity (η) and ϕ space, is shown in Figure 21a for a perfect calorimeter with no underlying event. It can be seen that the mass resolution improves with increasing cone size. However when running at high luminosity there are ≈<30> minimum bias events which accompany the event of interest. The fractional mass resolution as a function of cone size is plotted in Figure 21b.
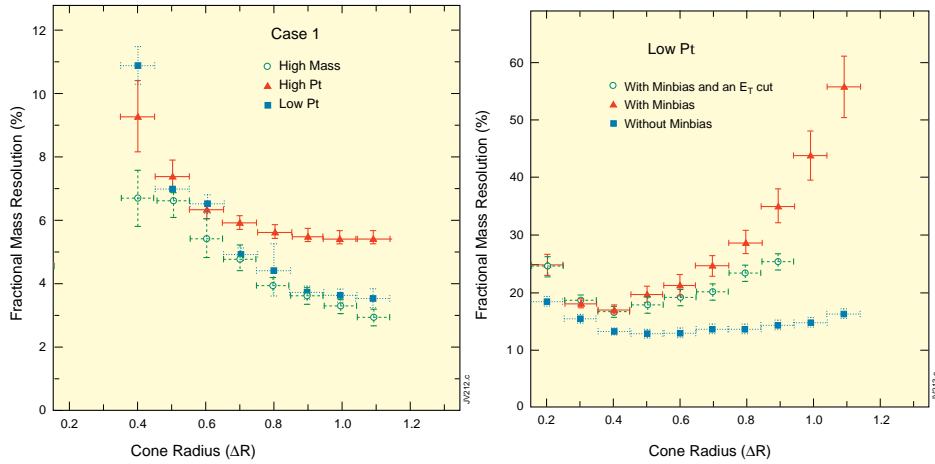

Figure 21: The fractional jet-jet mass resolution as function of cone radius a) perfect calorimeter, b) with 30 minimum bias events overlapped with the event of interest.

The mass resolution for low and high p_t di-jets is tabulated in Table 2 for different conditions.

When running at high luminosity at the LHC there are ≈ <25> minimum bias events that accompany the event of interest. The fractional mass resolution as afunction of the cone size is plotted in Figure 21.

Table 2: Mass resolution (in%) for low (top) and high p_t di-jets for different conditions (see text)

ΔR	Case 1	Case 2	Case 3	Case 4	Case 5
0.4	10.9	10.3	12.2	13.2	12.9
0.5	7.0	10.1	11.9	12.8	12.6
0.6	5.5	10.9	13.1	12.8	13.1
0.7	4.9	11.2	13.7	13.6	13.3
0.8	4.4	12.0	13.7	13.6	13.3
0.9	3.7	13.0	14.4	14.3	13.8
1.0	3.6	14.3	16.0	14.8	-

ΔR	Case 1	Case 2	Case 3	Case 4	Case 5
0.4	6.7	-	7.3	-	6.4
0.5	6.6	6.6	7.1	6.4	5.9
0.6	5.4	5.8	6.4	5.6	5.6
0.7	4.8	5.2	6.0	5.2	5.6
0.8	3.9	5.1	6.0	4.9	5.5
0.9	3.6	4.9	5.7	4.9	4.7
1.0	3.3	4.9	5.7	4.9	4.8

The cases are :
1: perfect colorimeter, no magnetic field, no underlying event,
2: + underlying event,
3: + energy resolution,
     ECAL – $\sigma/E=3\%/\sqrt{E}\oplus0.5\%$, HCAL: $\sigma/E=60\%/\sqrt{E}\oplus3\%$, e/h=1
4: + 4T magnetic field
5: + tower threshold (low p_t events – $E_t>0.3$ GeV, others $E_t > 1$ GeV)

From the above it can be seen that in hadronic colliders the uncertainties caused by jet fragmentation (fluctuation of energy inside a pre-defined cone size) and underlying event are very significant in comparison with instrumental effects such as energy resolution, magnetic field, threshold E_t etc.). Hence the mass resolution finally depends on the physics itself. At high luminosities the resolution is degraded if the cone-size is too small (some signal energy is excluded) or if the cone size is too large (significant pileup energy is included). In order to obtain the best mass resolution the cone size has to be optimised for each process and instantaneous luminosity.

6.5.3   *Di-jet Mass Resolution v/s Calorimeter Lateral Segmentation*

The mass resolution due to the angular error, dθ, in defining the jet axis is given by:

$$\frac{dM}{M} = \frac{p_T}{M} d\theta$$

Only highly boosted and low mass di-jets (e.g. boosted Zs from H→ZZ) will have a significant contribution from the angular error. This is illustrated in Figure 22 [19].
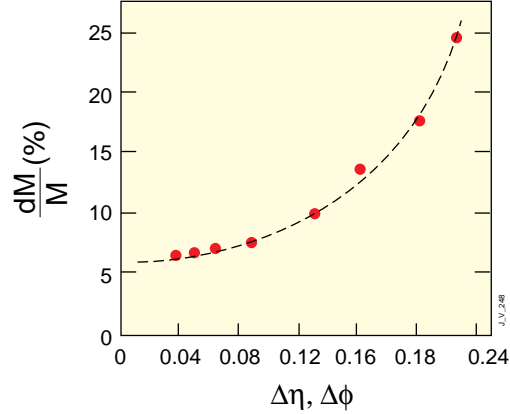

Figure 22: The fractional jet-jet mass resolution as a function of the tower size.

7. PARTICLE IDENTIFICATION USING CALORIMETERS

Several channels from potential new physics at the LHC may appear through final states containing leptons or photons e.g. some decay modes of the Higgs boson such as H→γγ or H→ ZZ* → 4l. Such modes have very small cross-sections in the range of 10-100 fb. However the backgrounds from QCD processes can be large. Hence a large rejection factor against the background is required while maintaining a high efficiency for the signal. Below we consider some ways in which calorimeters can be used to identify isolated electrons and photons from hadrons and jets.

7.1 Isolated electromagnetic shower-jet separation

The largest source of electromagnetic showers is from the fragments of jets, especially π^0s. A leading π^0 taking most of the jet energy can fake an isolated photon. There are large uncertainties in jet production and fragmentation. Furthermore the ratio of production of di-jets to irreducible di-photon background is $\approx 2.10^6$ and γ-jet/irreducible γγ is ≈ 800. Hence a rejection of ≈ 5000 against jets is needed.

Jets can be distinguished from single electromagnetic showers by
• demanding an energy smaller than some threshold in the hadronic compartment behind the electromagnetic one
• using isolation cuts

• demanding a lateral profile of energy deposition in the ECAL consistent with that from an electromagnetic shower.

Using these criteria ATLAS [7] estimates that the rejection factor against jets can be $\approx$ 1500 for a photon efficiency of 90%. This is illustrated in Figure 23 where the effect of various cuts is shown: a) the energy (E_T^{had}) in the hadron calorimeter compartment behind the e.m. one of size $\Delta\eta\times\Delta\phi$=0.2x0.2 should be less than 0.5 GeV, b) e.m. isolation (R_{isol})– more than 90% of the energy is contained in the central 3×5 e.m. cells compared with that in central 7×7 e.m. cells, c) lateral shower profile ($R_{lateral}$)– look for an e.m. core such that the central 4 towers contain more than 65% of the shower energy, d) shower width in η (σ_η). The distribution for jets is shown as dashed histogram whereas the full histograms depict single photons.
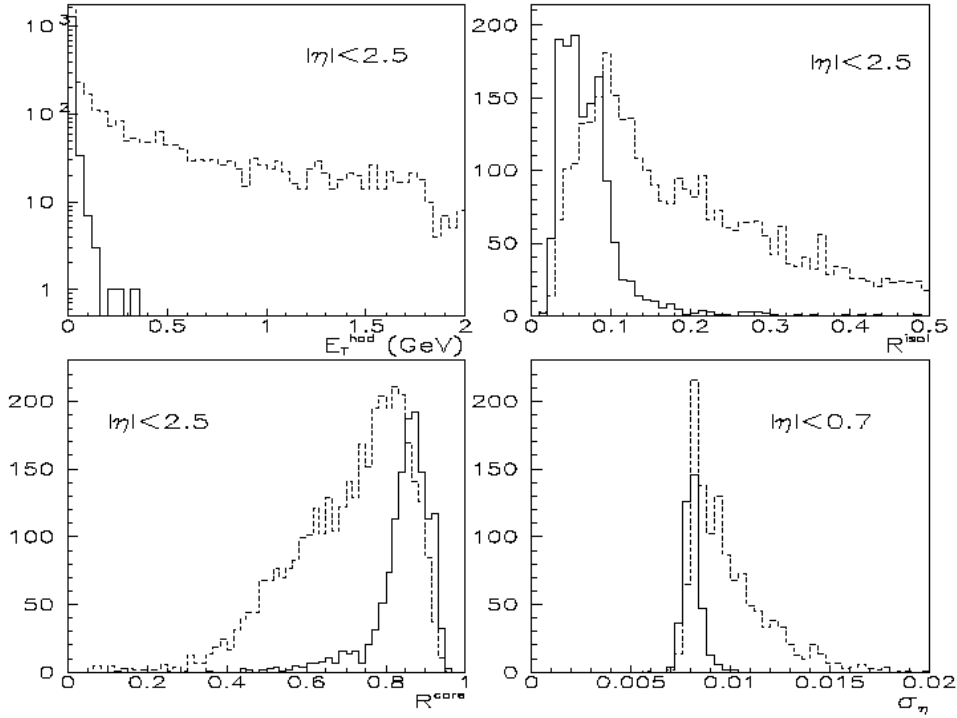

Figure 23: The distributions used to cut against jets. Solid histogram is for photons and the dashed one for jets. See text for explanation.

7.2   Photon – π^0 separation

After the application of the above criteria only jets resulting in leading π^0s can fake genuine single photons. Further rejection can only be achieved by the recognition of two e.m. showers close to each other. CMS [8] uses the fine lateral granularity ($\approx$2.2cm×2.2cm) of their crystals and a neural

network algorithm that compares the energy deposited in each of the 9 crystals in a 3×3 crystal array with that expected from a single photon. Variables are constructed from the 9 energies, x and y position of impact and a pair measuring the shower width. The fraction of π^0s rejected is shown in Figure 24.

The narrowness of the e.m. shower in the early part can be used to reject events consisting of two close-by e.m. showers. Planes of fine pitch orthogonal strips after a pre-shower, placed at a depth of $\approx 2.5\ X_0$, can also be used to distinguish π^0s from single photons. Results using 2mm pitch strips are shown in Figure 24.
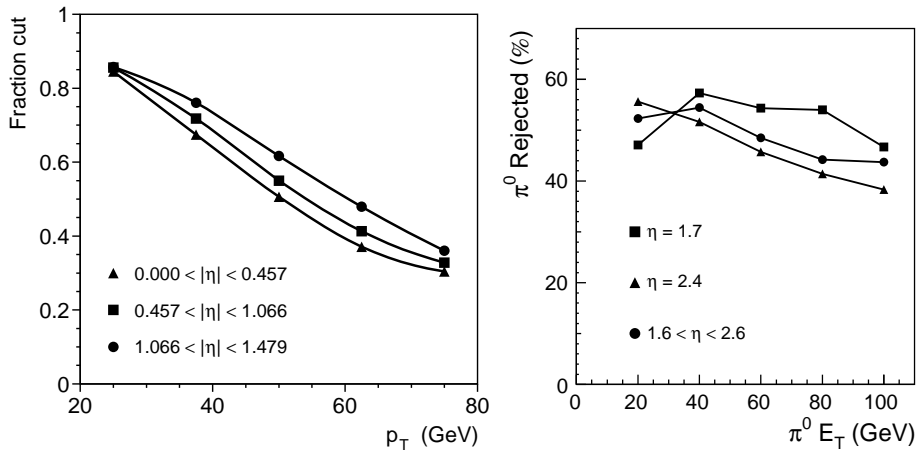

Figure 24: lhs) Fraction of pizeros rejected using lateral shape of energy deposit as a function of p_T rhs) Variation of pizero rejection as a function of η using two planes of orthogonally oriented 2mm pitch Si strips after 2 and 3 X_0.

Electron-hadron Separation

A high energy pion faking an electron leads to the contamination of signals using prompt electrons. At LHC in order to bring down the rate of fake electrons from this source to a factor ≈ 10 below that from the genuine sources (e.g. b –> e X, W –> eν etc.) an e-π separation of ≥ 1000 is required for $p_T \geq 10$ GeV/c.

The electron–hadron separation is usually based on the difference in the longitudinal and lateral development of showers intiated by electrons and charged hadrons. One or more of the following can be used to achieve the desired pion rejection power when detecting electrons :
• a preshower detector between $\approx 1.5 - 4\ X_O$

• lateral segmentation
• longitudinal segmentation including a hadron calorimeter
• energy - momentum matching

The ultimate rejection power is limited by the charge exchange process or the first hadronic interaction, which results in one or several π^0's taking most of the energy of the incoming hadron. The shower from such hadrons then looks like an e.m. shower. Therefore sampling of showers early in their longitudinal development is important.

The separation power for single particle, using (i - iii) is shown in Figure 25 [20]. The structure of the calorimeter consisted of :
• towers of a lateral size of ~11 x 11cm (effective $X_O \approx$ 8mm),
• 8-fold longitudinal segmentation, the first four samplings (2mm U / 2.5 mm TMP) with thickness of 3, 6, 10, 7 X_O leading to a total of 1λ, the next two (5mm U/ 2.5mm TMP) each with thickness of 0.7 λ and the last two (5cm Fe/ 1cm scintillator) each with thickness of 2.5 λ.
• a position detector placed at a depth of 3 Xo.
The rejection power, as a function of energy, using (ii), (iii) and (iv) individually and then all combined is shown.
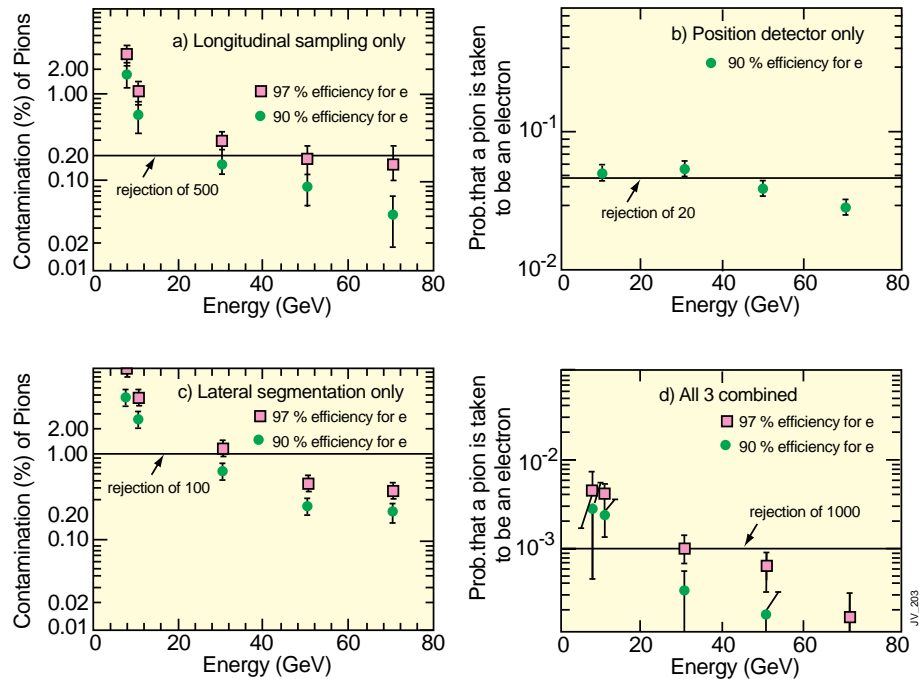

Figure 25: The probability that a single pion is taken to be an electron using a) longitudinal profile only, b) preshower detector only, c)lateral profile only and d) all three combined.

8. ELECTRONICS NOISE

Noise is any unwanted signal that obscures the desired signal. Therefore noise degrades the accuracy of the measurement. There are two types of noise: *intrinsic* and *extrinsic* noise. The intrinsic noise is generated in the detector or electronics and cannot be eliminated though possible reduced. The extrinsic noise is due to pickup from external sources or unwanted feedback (e.g. ground loops, power supply fluctuations etc.) and is usually eliminated by proper design.

Intrinsic noise has two principal components namely :
• thermal noise (Johnson or Nyquist noise) – *series noise*
Any resistor, R, will develop a voltage across its ends whose average value is zero but r.m.s. is

$$\langle v^2 \rangle \;=\; 4ktR.\Delta f$$

• shot noise – *parallel noise*
This source arises from fluctuation in the charge carriers and is given by

$$ENC^2 \;=\; \frac{4ktR_s(C_d + C_{in})^2}{\tau}\; I_s \;+\; I_n\; \tau\; I_p$$

where C_d is detector capacitance, C_{in} is input capacitance of the amplifier, I_n is leakage current, τ is the shaping time and I_s, I_p are series and parallel noise integrals (≈ 1 for $(RC)^2$ shaping). For example, for $\tau = 50$ ns, and a leakage current of 1 µA, ENC ≈ 800 electrons. Further examples are considered in Sections 9.3 and 10.2.

9. INORGANIC SCINTILLATORS

The desirable properties of a scintillator are:
• a high efficiency of conversion of deposited energy into scintillation light,
• a conversion to light that is proportional to the energy deposited,
• a high light output,
• a medium that is transparent to its emitted light,
• a short luminescence decay time,
• a refractive index n $\approx$ 1.5 for efficient coupling to photosensors
• radiation hardness for LHC operation.

No material simultaneously meets all these criteria. Inorganic scintillators (e.g. sodium iodide) have the best light output and linearity whilst organic scintillators (e.g. plastic scintillator) have faster light output but smaller light yield and display saturation of output for radiation with high linear energy transfer. Two types of light emission are possible: *fluourescence*

resulting in prompt emission of light in the visible wavelength range and *phosphorescence* resulting in slower emission of light at longer wavelengths.

The most demanding physics channel for an electromagnetic calorimeter at the LHC is the two-photon decay of an intermediate-mass Higgs boson. The background is large and the signal width is determined by the calorimeter performance. The best possible performance in terms of energy resolution only possible using fully active calorimeters such as inorganic scintillating crystals.

Inorganic scintillators have crystalline structure. The valence band contains electrons that are bound at the lattice sites whereas electrons in the conduction band are free to move throughout the crystal. Usually in a pure crystals the efficiency of scintillation is not sufficiently large. A small amount of impurity, called an activator, is added to increase the probability of emission of visible light. Energy states within the forbidden gap are created through which an electron, excited to the conduction band, can de-excite. Passage of a charged particle through the scintillator creates a large number of electron-hole pairs. The electrons are elevated to the conduction band whereas the +ve holes quickly drift to an activator and ionize it. The electrons migrate freely in the crystal until they encounter ionised activators. The electrons drop into the impurity sites creating activator excited energy levels which de-excite typically with $T_{1/2} \approx 100$ ns. In a wide category of materials the energy required to create an electron-hole pair is $W \approx 3E_g$ e.g. in NaI, $W \approx 20$ eV, NaI(Tl) $N_\gamma \approx 40000\gamma$/MeV of ≈ 3 eV.
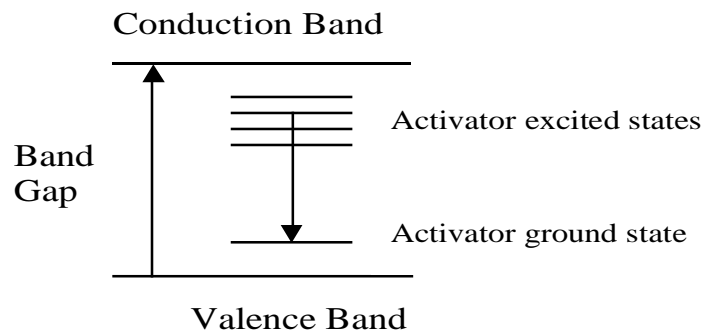

Figure 26: The energy level diagram for a scintillating crystal containing an activator

The consequence of luminescence through activator sites is that the crystal is transparent to its own scintillation light. In this case the emission and absorption bands do not overlap and self-absorption is small. The shift towards longer wavelengths is known as *Stokes' shift*.

The scintillation mechanism in crystals without activators is more complex. For example, in lead tungstate the intrinsic emission in the blue is through excitons localized on the Pb site whereas the green emission is due to defects in the crystalline structure linked to oxygen vacancies [21].

The properties of various crystals used in high energy experiments are given in Table 3. The parameters of some of the recently designed crystal calorimeters are given in Table 4 [22].

Table 3: Properties of various scintillating crystals.

Crystal	NaI(Tl)	CsI(Tl)	CsI	BaF$_2$	BGO	CeF$_3$	PbWO$_4$
Density g.cm^{-2}	3.67	4.51	4.51	4.89	7.13	6.16	8.28
Rad. length cm	2.59	1.85	1.85	2.06	1.12	1.68	0.89
Moliére radius cm	4.5	3.8	3.8	3.4	2.4	2.6	2.2
Int. length cm	41.4	36.5	36.5	29.9	22.0	25.9	22.4
Decay Time ns	250	1000	35 6	630 0.9	300	10-30	<20>
Peak emission nm	410	565	420 310	300 220	480	310- 340	425
Rel. Light Yield %	100	45	5.6 2.3	21 2.7	9	10	0.7
d(LY)/dT %/^{0}C	≈ 0	0.3	- 0.6	- 2 ≈ 0	- 1.6	0.15	-1.9
Refractive Index	1.85	1.80	1.80	1.56	2.20	1.68	2.16

Table 4: Parameters of various experiments using scintillating crystals.

Experiment		KTeV	BaBar	BELLE	CMS
Laboratory		FNAL	SLAC	KEK	CERN
Crystal Type		CsI	CsI(Tl)	CsI(Tl)	PbWO$_4$
B-Field	T	-	1.5	1.0	4.0
Inner Radius	m	-	1.0	1.25	1.3
No. of crystals		3,300	6,580	8,800	76,150
Crystal Depth	X$_0$	27	16-17.5	16.2	26
Crystal Volume	m^3	2	5.9	9.5	11
Light Output p.e./MeV		40	5,000	5,000	2
Photosensor		PMT	Si PD	Si PD	APD*
Gain of photosensor		4,000	1	1	50
Noise / channel MeV		Small	0.15	0.2	30
Dynamic Range		10^4	10^4	10^4	10^5

* APD: Si avalanche photodiode

9.1 Radiation Damage in Crystals

All crystals suffer from radiation damage at some level. It is rare that irradiation affects the scintillation mechanism itself. However formation of colour centres takes place leading to absorption bands. A colour centre is a crystal defect that absorbs visible light. A high concentration of blue light colour centres makes crystals yellowish. The simplest colour centre is an F-centre where an electron is captured in an anion vacancy. The consequence of colour centre production is a decrease in the light attenuation length leading to a decrease in the amount of light incident on the photosensor. This is illustrated in Figure 27 for various samples of $PbWO_4$ crystals grown under differing conditions. The crystals were irradiated using γs, incident at the front of the crystal, from a ^{60}Co source.
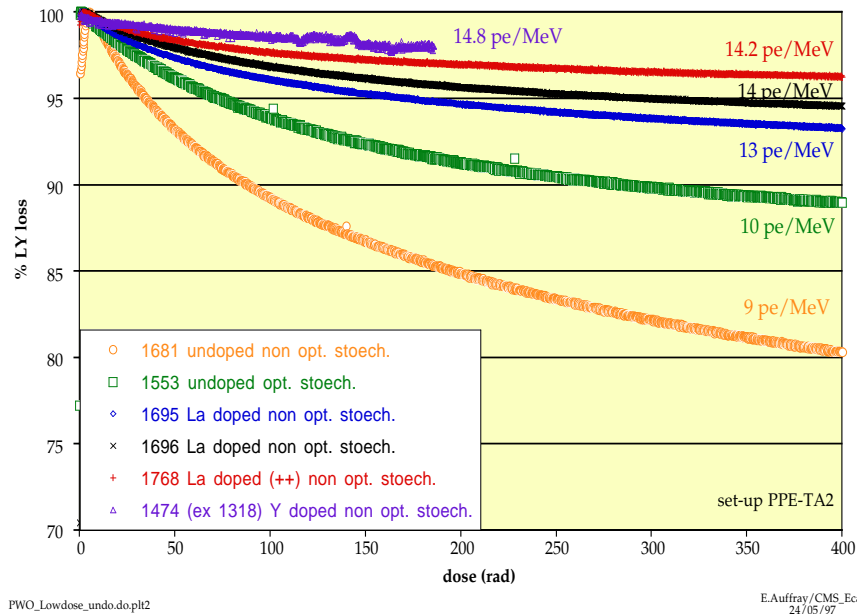

Figure 27: The loss in the collected light as a function of dose (delivered at ≈ 0.15 Gy/hr) for crystals grown under various conditions.

Extensive R&D has been carried out over the last 5 years in order to improve the radiation hardness of $PbWO_4$ crystals [21]. Generally the strategy has been to decrease the concentration of defects that lead to colour centre production by optimizing the stoichiometry (the concentration of PbO and WO_3 in the melt) and annealing after the growth of the crystal. The remaining defects are compensated by specific doping, e.g. by pentavalent elements on the W site and trivalent on the Pb site, and by improving the purity of the raw materials. The levels of improvement can be seen from Figure 27. The most recent crystals of lead tungstate have shown very good

resistance to irradiation. This is illustrated in Figure 28. The loss of collected light, for crystals doped with both niobium and yttrium, show a decrease in the collected light of less than 2% at saturation. The effect of irradiation can also be dose-rate dependent.
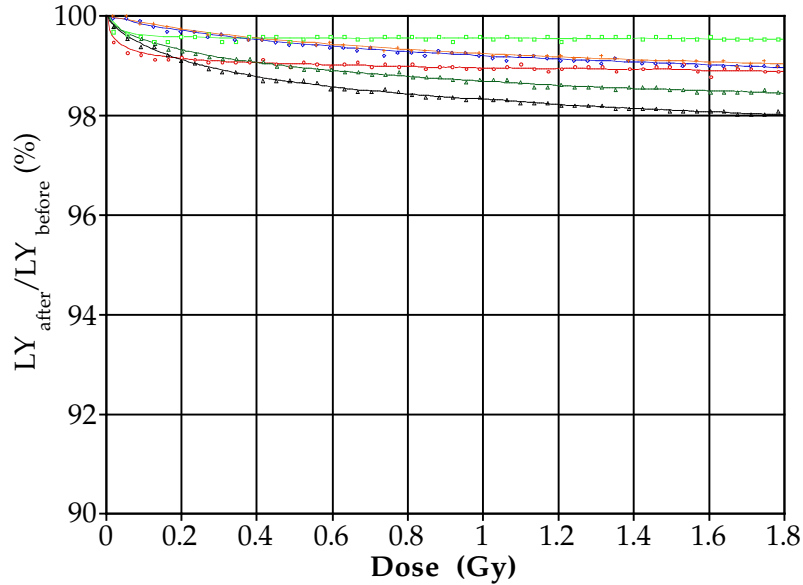

Figure 28: The loss in the collected light as a function of dose (delivered at $\approx$ 0.15 Gy/hr) for recent $PbWO_4$ crystals doped with Niobium and Yttrium.

The radiation dose expected at the shower maximum for the lead tungstate calorimeter of CMS, over the first ten years of LHC operation, is below 4,000 Gy in the barrel region ($|\eta| < 1.5$), $\approx$ 70,000 Gy at $|\eta| \approx 2.5$ rising to 200,000 Gy at $|\eta| \approx 3.0$. Furthermore the expected dose rate at design luminosity, and shower maximum, is below 0.3 Gy/h in the barrel region, $\approx$ 6 Gy/h at $|\eta| \approx 2.5$ rising to 15 Gy/h at $|\eta| \approx 3.0$.

9.2   Performance of CMS Lead Tungstate Crystals

Several matrices of improving quality have been tested in electron beams over the last few years [23,24]. Radiation damage leads to a decrease in the attenuation length and hence in the collected light. As the efficiency of the scintillation mechanism is not affected by irradiation the energy resolution will not be affected as long as the attenuation length does not fall below $\approx$ 2-3 time the length of the crystal. The small loss of light can be corrected by regularly measuring the response to a known amount of light injected into crystals. This has been demonstrated in beam tests [24].

Results from a recently tested prototype are shown in Figure 29. The distribution of the sum of energy in 9 crystals for electron of an energy of 280 GeV is shown. An excellent energy resolution is measured without significant tails. The measured energy resolution is also shown. The stochastic term is expected to be < 3% in the final calorimeter since the surface area of the photosensor will be doubled. This should result in physics performance described in another contribution [25] in this school.
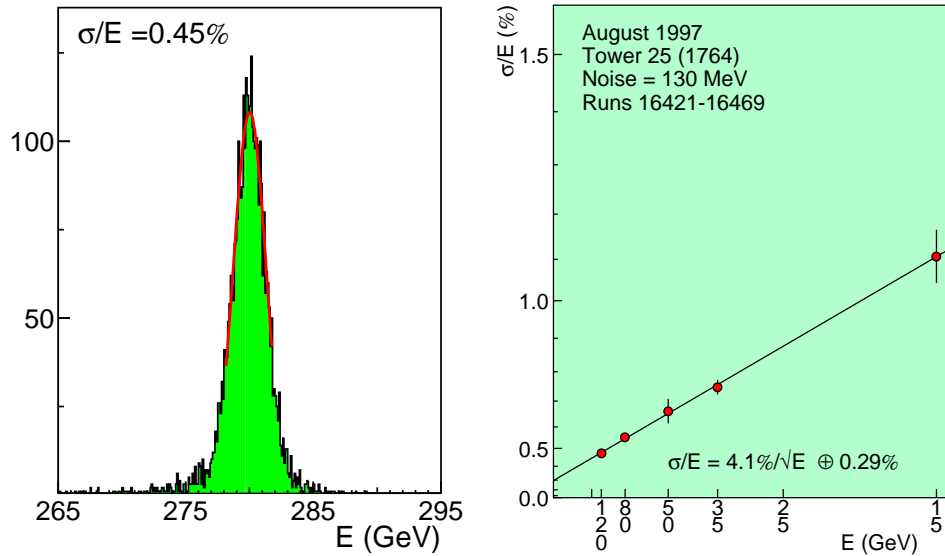

Figure 29: a) The distribution of the sum of energy in 9 crystals for an electron of an energy of 280 GeV, b) the measured energy resolution

9.3 Photosensors

9.3.1 Photomultipliers

The contribution to the energy resolution from the process of conversion of light to photoelectrons can be significant. For example, in a lead glass calorimeter about 10,000 Cerenkov photons/GeV impinge on the photomultiplier. The conversion leads to about 1000 photoelectrons/GeV and hence the contribution to the stochastic term will be

$$\sigma_{pe} = \frac{\sigma}{E} = \frac{\sqrt{1000}}{1000} \approx 3.2\%$$

The maximum number of independent $e^{\pm}$ particles, given that the Cerenkov threshold is 0.7 MeV, is 1000/0.7 per GeV i.e. n = 1400 $e^{\pm}$. This leads to an additional contribution to the energy resolution i.e. $\sigma_n = (\sqrt{1400})/1400 \approx$ 2.7%. The observed resolution then becomes

40

$$\frac{\sigma}{E} = \sqrt{\sigma_n^2 + \sigma_{pe}^2} \approx 4.5\%$$

An energy resolution of $\sigma/E \sim 5\% / \sqrt{E}$ for e.m. showers has been attained in a large lead glass array [26].

9.3.2 Silicon Avalanche Photodiodes

The light output from $PbWO_4$ crystals is low. These crystals are deployed by CMS in a 4T transverse magnetic field and the use of photomultipliers is excluded. Unity gain Si photodiodes cannot be used since even the small rear shower leakage from 25 X_0 deep crystals considerably degrades the energy resolution [23]. This is due to the fact that the response to ionising radiation is significant compared to the signal due to scintillation light. Hence CMS use Si avalanche photodiodes (APDs) with a gain of about 50. The particularity of these devices, over and above photomultipliers, is the noisy amplification process. The working principle of these devices is shown in Figure 30.
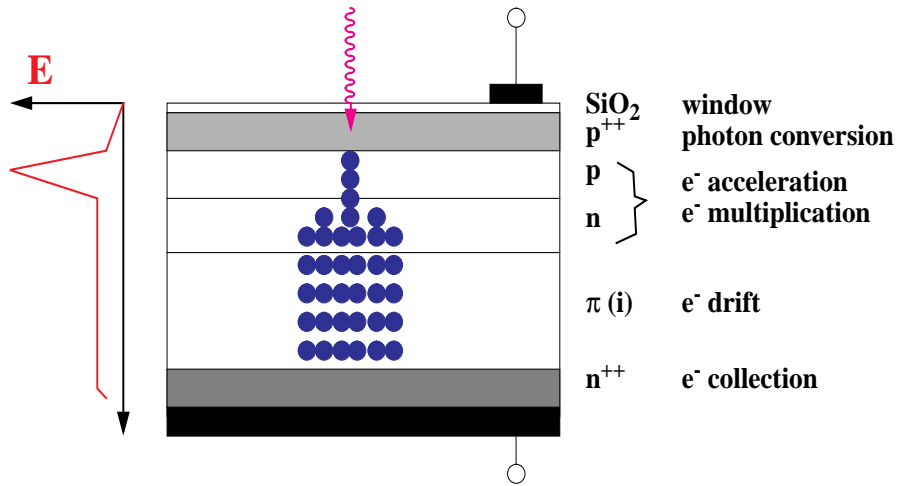

Figure 30: The working principle of a Si avalanche photodiode.

Consider a crystal with a light yield of N_γ photons/MeV. $N_\gamma.E$ photons hit the APD for an energy deposit E. Assuming a quantum efficiency Q (which can easily be $\approx 85\%$ for APDs),

No. of photoelectrons is $\qquad\qquad N_{pe} = N_\gamma.E.Q$

Then the photostatistics fluctuation is $\qquad \pm\sqrt{N_{pe}}$

If there is no fluctuation in the gain process then the no. electrons transferred to the amplifier is (M=gain) $\qquad M.N_{pe} \pm M\sqrt{N_{pe}}$

BUT if the multiplication process is noisy and the gain itself has a fluctuation, σ_M, then the no. of electrons is $\quad M.N_{pe} \pm \sqrt{(M^2 + \sigma_M^2)}\sqrt{N_{pe}}$

Hence the photostatistics contribution to the energy resolution becomes

$$\frac{\sigma_{pe}(E)}{E} \;=\; \frac{1}{\sqrt{N_\gamma E Q}}\sqrt{\frac{M^2 + \sigma_M^2}{M^2}} \;=\; \frac{1}{\sqrt{N_\gamma E Q}}\;\sqrt{F}$$

where F is called the 'excess noise factor' and quantifies the induced degradation in the energy resolution due to fluctuations in the amplification process. Typically for APDs F≈ 2 and for photomultipliers F ≈ 1.2.

Another source of energy resolution degradation arises when APDs are damaged by irradiation. APDs behave as conventional Si devices under irradiation and the leakage current increases with the same damage constant ($\alpha = 2.10^{-17}$ A/cm). The leakage current can have two sources: surface and bulk current. The surface leakage (I_s) current does not undergo multiplication whereas the bulk current generated in the amplification region (I_b) does.

For I_s, if electrons flow at a rate of 1 e/s, but arrive randomly, then $\sigma_s\,\alpha\,\sqrt{I_s}$. For I_b, because of amplification, the fluctuation is $\sigma_b\,\alpha\,M\,\sqrt{(FI_b)}$
Incorporating the effect of fluctuation in gain into the energy resolution yields

$$\frac{\sigma_{pe}(E)}{E} \;=\; \frac{a}{\sqrt{E}} \oplus \frac{b}{E} \oplus \sqrt{\frac{F}{N_\gamma E Q}} \oplus \alpha\,\frac{"C"\sqrt{"R"}}{M N_\gamma E Q \sqrt{\tau}} \oplus \beta\,\frac{\sqrt{I_s + M^2 F I_b}}{M N_\gamma E Q}\;\sqrt{\tau}$$

where "C" is the total capacitance at the input and "R" is the input transconductance + photodetector series resistance.

Some properties of APDs, from two manufactures, are listed in Table 5.

<div align="center">Table 5: Some properties of APDs</div>

Parameter	Hamamatsu	EG&G
Active Area	25 mm^2	25 mm^2
Quantum Efficiency at 450nm	80%	75%
Capacitance	100 pF	25 pF
Excess Noise Factor, F	2.0	2.3
Operating Bias Voltage	400-420 V	350-450 V
dM/dV x 1/M at M=50	5%	0.6%
dM/dT x 1/M at M=50	-2.3%	-2.7%
Passivation Layer	Si$_3$N$_4$	Si$_3$N$_4$

9.4   System Aspects
A real calorimeter is a system comprising active media, electronics chain, mechanical structure, all enclosed in an environment that must be kept

stable. Hence many other factors have to be considered in order to maintain the resolution achieved in beam tests. For example, in the case of the CMS ECAL, the temperature of the crystals has to be maintained to within 0.1% since both the crystal and the photosensor have a temperature dependence of the output signal of $d(Signal)/dT \approx -2\%/{}^{0}C$. This requires a powerful cooling system and a hermetic environmental shield. To maintain uniformity of response across crystals the mechanical structure has to be thin and preferably made of low-Z material. Furthermore, no load from one crystal should be transferred to its neighbours. A 300 μm glass fibre alveolar structure has been chosen by CMS. The electronics system has to provide a stable response, deliver high resolution of digitization (12-bits) and a large dynamic range ($\approx$16-bits) whilst preserving a low electronics noise per channel (<40 MeV/channel). Furthermore, the on-detector electronics must be radiation hard and have as low a power consumption as possible.

More information on the systems aspects of calorimeters can be found in the ATLAS [7] and CMS [8] Technical Design Reports.

10   CALORIMETRY USING NOBLE LIQUIDS

Calorimeters using liquid filled ionization chambers as detection elements have several important advantages. The absence of internal amplification of charge results in a stable calibration over long periods of time provided that the purity of the liquid is sufficient. The number of ion pairs created is large and hence the energy resolution is not limited by primary signal generating processes. The considerable flexibility in the size and the shape of the charge collecting electrodes allows high granularity both longitudinally and laterally.

 The desirable properties of liquids used in ionization chambers are:
• a high free electron or ion yield leading to a large collected charge,
• a high drift velocity and hence a rapid charge collection,
• a high degree of purity. The presence of electron scavenging impurities leads to the reduction of electron lifetime and consequently a reduction in the collected charge.

The properties of noble liquids are given in Table 6.

10.1   Charge Collection in Ionisation Chambers

Ionisation chambers are essentially a pair of parallel conducting plates separated by a few mm and with a potential difference in an insulating liquid (e.g. liquid argon).

Consider what happens when a single ion-pair is created at a distance (d-x) from the +ve electrode (Figure 31a). The electron drifts towards the +ve electrode and induces a charge

$$Q = -e \frac{(d-x)}{d}$$

where d is the width of the gap. Assuming that the electron drifts with a velocity v, and the time to cross the full gap is v_d, then the induced current is

$$i(t) = \frac{dQ}{dt} = -e \frac{v}{d} = -\frac{e}{t_d}$$

The contribution from the drifting ions can be neglected as their drift velocity is about three orders of magnitude smaller than that for electrons.

Table 6: Properties of noble liquids.

		LAr	LKr	LXe
Density	g/cm^3	1.39	2.45	3.06
Radiation Length	cm	14.3	4.76	2.77
Moliere Radius	cm	7.3	4.7	4.1
Fano Factor		0.11	0.06	0.05
Scintillation Properties				
Photons/MeV		-	$1.9 \cdot 10^4$	$2.6 \cdot 10^4$
Decay Const. Fast	ns	6.5	2	2
Slow	ns	1100	85	22
% light in fast component		8	1	77
λ peak nm		130	150	175
Refractive Index @ 170nm		1.29	1.41	1.60
Ionization Properties				
W value	eV	23.3	20.5	15.6
Drift vel (10kV/cm)	cm/μs	0.5	0.5	0.3
Dielectric Constant		1.51	1.66	1.95
Temperature at triple point	K	84	116	161

Now consider the case where a charged particle traverses the gap (Figure 31b). Suppose N ion-pairs are produced and are uniformly distributed across the gap. The fraction of electrons still moving at a time t after traversal is $(t_d$-t)/t_d$ for $t_d < t$. Therefore

$$i(t) = -Q_0 \frac{v}{d} \left(1 - \frac{t}{t_d}\right)$$

where $Q_0 = Ne$ and the current is at its maximum at time $t = 0$ and disappears once all the charges have crossed the drift gap. This time is about 400 ns for a 2 mm LAr gap.Hence

$$q(t) = \int_0^t i(t) \ dt = -Q_0 \left(\frac{t}{t_d} - \frac{t^2}{2t_d^2} \right) \quad for \ t < t_d$$

The total collected charge (for $t > t_d$) is

$$Q_c = \frac{Q_0}{2}$$

The factor two is due to uniform distribution of ionisation. During drift the electrons can be trapped by impurities. Then the induced current will be reduced. In fact if the electron lifetime is τ

$$i(t) = \frac{Q_0}{t_d} \left(1 - \frac{t}{t_d} \right) e^{-t/\tau} \quad for \ t < t_d$$
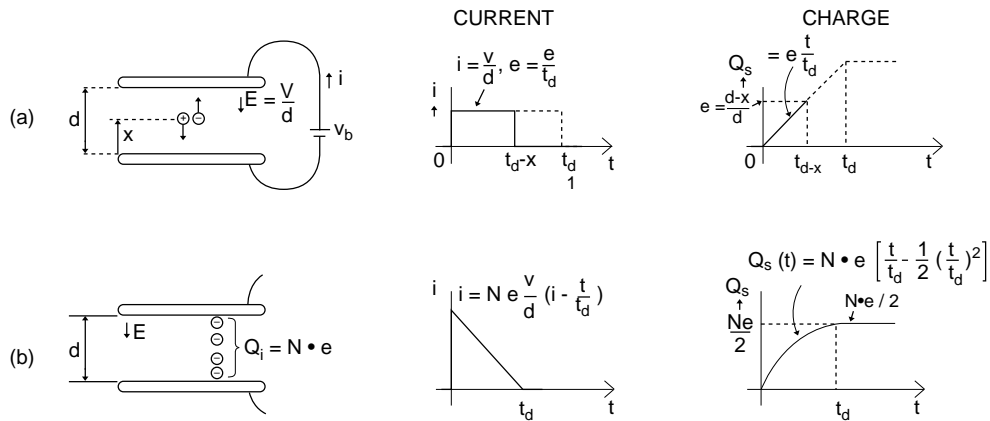

Figure 31: The distributions for the current and charge for a) a single e-ion pair, b) uniformly distributed e-ion pairs.

10.2   Signal Shapes

As discussed above, for a long electron 'lifetime' the induced current has a triangular shape with a duration equal to the electron drift time t_d (Figure 32a [15]). The total collected charge is also shown. It is clear that a device based on full charge collection will be slow, and hence not suitable for use at the LHC. However the energy information is contained in the initial current i_0. The information can be extracted and high rate operation established by clipping the signal with a fast bipolar shaping (Figure 32b). If the system impulse response has zero integrated area then pileup does not

produce a baseline shift. For a peaking time, t_p that is much faster than drift time i.e. $t_p \ll t_d$, the output response becomes the first derivative of the current pulse (Figure 32c). The height of the output pulse is proportional to the initial current. However, with respect to full charge collection, the energy equivalent of the electronics noise will increase as this scales with $1/\sqrt{\tau}$, where τ (=RC) is the shaper time constant. At high luminosities, pileup also influences the choice of the value of τ. Pileup scales as $\sqrt{\tau}$. As an example, the optimized value for τ gives $t_p \approx 40$ ns for the ATLAS "accordion" e.m. calorimeter..
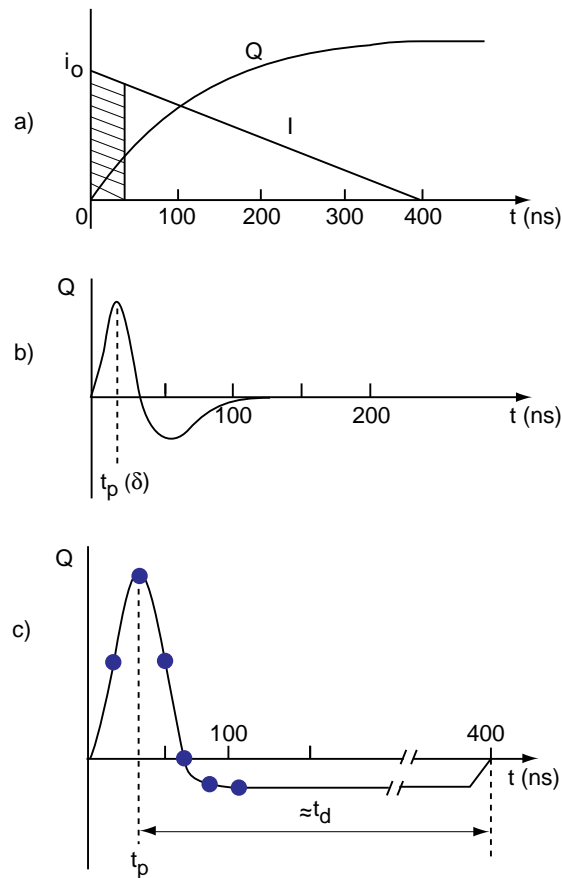
Figure 32: a) Induced current and integrated charge, b) bipolar shaping function and c) the shape of the output pulse, all as a function of time.

10.3 Examples of Noble Liquid Calorimeters

Conventionally ionization chambers are oriented perpendicularly to the incident particles. However in such a geometry it is difficult to
- realize fine lateral segmentation with small size towers, which in addition need to be projective in collider experiments,

- implement longitudinal sampling,

without introducing insensitive regions, a large number of penetrating interconnections, and long cables which necessarily introduce electronics noise and lead to significant charge transfer time. To overcome these shortcomings a novel absorber-electrode configuration, known as the 'accordion' (Figure 33, [27]), has been introduced, in which the particles traverse the chambers at angles around 45^0.
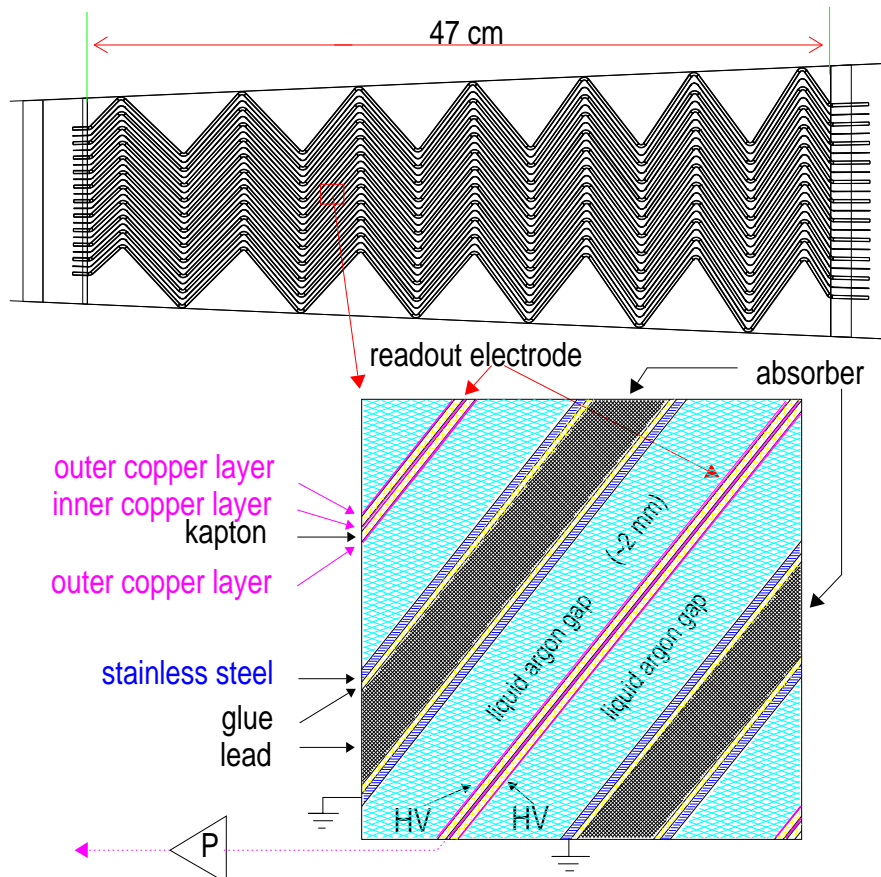

Figure 33: Top) the "accordion" structure of absorber plates of the ATLAS ECAL, below) details of the electrode structure.

In a variant, the NA48 [28] experiment has chosen an arrangement of electrodes that is almost parallel to the incident particles. With such structures the electrodes can easily be grouped into towers at the front or at the rear of the calorimeters. In ATLAS the absorber is made of lead plates, clad with thin stainless steel sheets for structural stiffness and corrugated to the shape shown in Figure 33. Details of the sampling structure are also shown. The read-out electrodes are made out of copper clad kapton flexible foil and kept apart from the lead plates by a honeycomb structure.
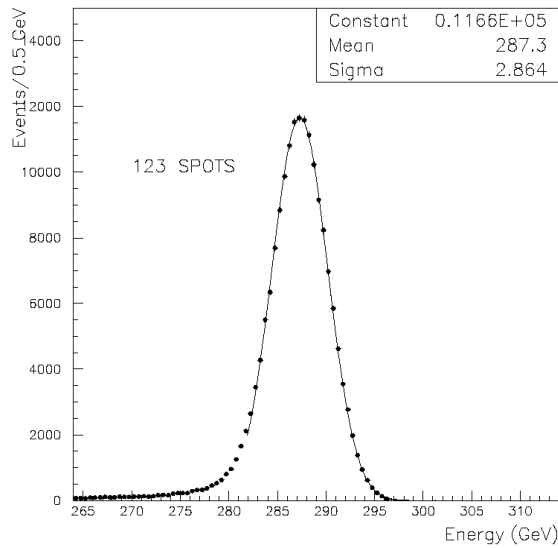
Figure 34: The distribution of the reconstructed energy for 300 GeV electrons in the ATLAS ECAL.
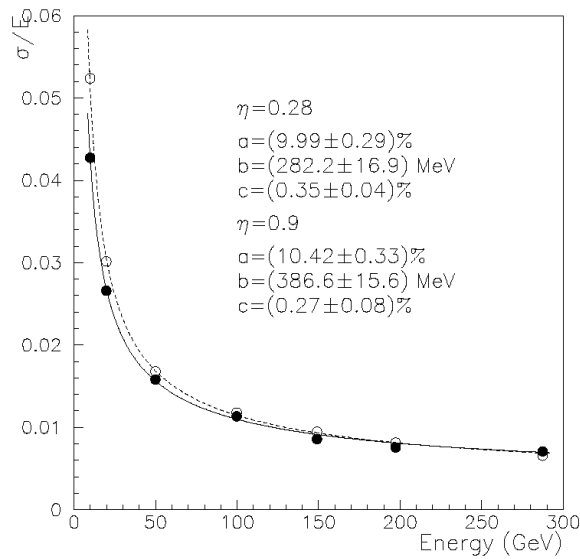

Figure 35: The fractional energy resolution for the ATLAS barrel prototype ECAL.

The results from a beam test of a large ATLAS prototype are shown in Figures 34 and 35. The electron shower is reconstructed using a region of 3x3 cells each of a size of ≈ 3.7 cm x 3.7 cm. The distribution of reconstructed energy for 300 GeV electrons, over a large area, is shown in Figure 34. The fractional energy resolution is shown in Figure 35 and can be parameterised as

$$\frac{\Delta E}{E} \approx \frac{10\%}{\sqrt{E}} \oplus \frac{0.28_{GeV}}{E} \oplus 0.35\%$$

where E is in GeV. The response of more than 150 cells over a large area has also been measured. The cell-to-cell non-uniformity is measured to be ≈0.58%. The major contributions come from mechanics (residual φ-modulation, gap non-uniformity, variation of absorber thickness) and calibration (amplitude accuracy). The large flux of isolated electrons from W or Z decays will be used to establish cell-to-cell intercalibration.

COMBINED E.M. AND HADRONIC CALORIMETRY

The LHC pp-experiments have put more emphasis on high precision e.m. calorimetry. This is not compatible with perfect compensation. For example the electromagnetic energy resolution of the ZEUS U-calorimeter is modest. The e.m. (σ_E) and hadronic (σ_h) resolutions are given by

$$\frac{\sigma_E}{E} = \frac{17\%}{E} \quad and \quad \frac{\sigma_h}{E} = \frac{35\%}{E}$$

Nevertheless it is very important to ensure:
• a Gaussian hadronic energy response function (a moderate energy resolution is acceptable),
• hermiticity
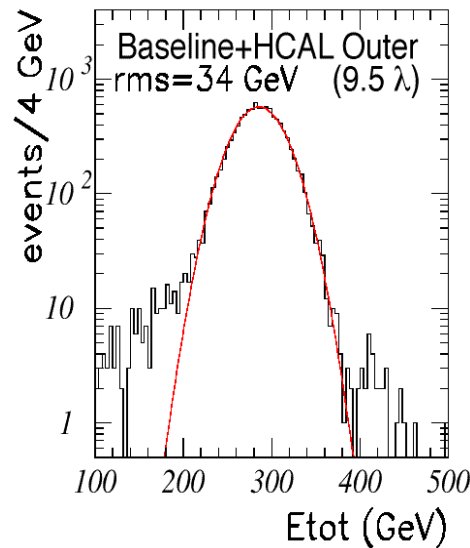• linearity of response, especially for jets.

Figure 36: Distribution of reconstructed energy of 300 GeV pions [8, HCALTDR].

As an example in CMS this is done by introducing multiple longitudinal samplings. Reading out separately the first scintillator plate, placed behind

the e.m. calorimeter, allows to distinguish between the cases where an e.m. shower has developed in the crystals (little signal from the first scintillator) and the ones where a hadronic shower has started (signal from the first scintillator). The energy observed in the first scintillator serves to make a correction. Infact the correction can be somewhat 'hard-wired' by choosing an appropriate thickness for the scintillator. The longitudinal leakage can also be up-weighted by increasing the thickness of the last scintillator. The measured energy distribution for 300 GeV pions in the CMS baseline is shown in Fig. 36. The tails are kept below a few percent.

The test beam results of the combined calorimetry of ATLAS (LAr ECAL and Fe/Scintillator HCAL) are shown in Figure 37. The data are compared with results from two simulation codes namely Fluka and GCALOR. Use is made of three energy-independent corrections for the:
• intercalibration between the e.m. and hadronic calorimeter
• energy lost in the cryostat wall separating the two calorimeters
• non-compensating behaviour of the e.m. calorimeter. A quadratic correction is made.
The above procedure minimizes the fractional energy resolution resulting in a systematic underestimation of the reconstructed energy: by 20% at 30 GeV and decreasing to ≈10% at 300 GeV. Other weighting methods, which have the effect of simultaneously minimizing the non-linearity and the energy resolution can also be employed.
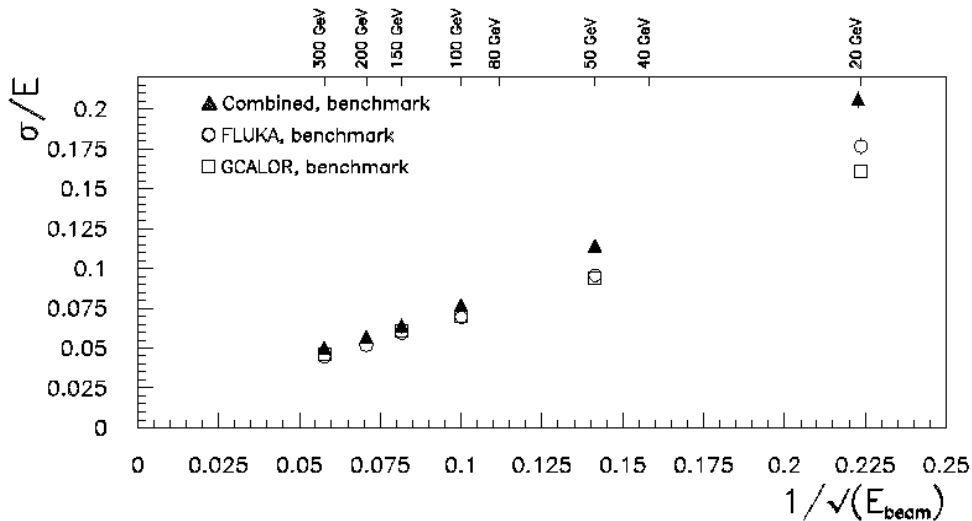

Figure 37: The energy resolution for pions compared with FLUKA and GCALOR simulation codes.

The hadronic cascade simulation codes such as FLUKA, GHEISHA and GCALOR have improved substantially and can now be used with some confidence in the design of hadron calorimeters.

CONCLUSIONS

Calorimeters are key detectors in present day high energy physics experiments. Large precision electromagnetic calorimeters are operating well (CLEO, KTeV, NA48), will soon be commissioned (BaBar, BELLE) or are under construction (ATLAS, CMS). High performance combined e.m. and hadronic calorimeters are also operating at DESY (H1 and ZEUS). Calorimeter systems have played a major role in many of the recent discoveries in particle physics e.g. W,Z in UA1/UA2, top quark in CDF/D0 and undoubtedly will play a similarly crucial role in the next generation of experiments at e^+e^- and p-pbar/pp machines.

Acknowledgements

References

1. U. Amaldi, *Exptl. Tech. In High Energy Physics*, p. 257, ed. T. Ferbel, Addison Wesley, 1987. Also in *Phys. Scripta* **23**(1981)409.

2. C. W. Fabjan, *Exptl. Tech. In High Energy Physics*, p. 325, ed. T. Ferbel, Addison Wesley, 1987.

3. R. Wigmans, *Ann. Rev. Nucl. And Part. Sci.* **41**(1991)133.

4. C. W. Fabjan and R. Wigmans, CERN-EP/89-64 (1989).

5. T. S. Virdee, Proc. 2nd Intl. Conf. On Calorimetry in High Energy Physics, p3, Capri, 1991, ed. A Ereditato, World Scientific.

6. R. Wigmans, Proc. 2nd Intl. Conf. On Calorimetry in High Energy Physics, p24, Capri, 1991, ed. A Ereditato, World Scientific.

7. ATLAS Technical Design Reports: Liquid Argon Calorimeter, CERN/LHCC/96-?? (1996), Tile Calorimeter, CERN/LHCC/96-42 (1996), http://atlasinfo.cern.ch/Atlas/GROUPS/notes.html

8. CMS Technical Design Reports, Electromagnetic Calorimeter, CERN/LHCC 97-33 (1977), Hadron Calorimeter, CERN/LHCC 97-31 (1997), http://cmsdoc.cern.ch/LHCC.html

9. Review of Particle Physics, C. Caso et al., *Euro. Phys. Journal* **C3**(1998)1, http://pdg.lbl.gov/

10. D. Barney, private communication.

11. M. De Vincenzi et al., WA78, *Nucl. Instr. and Meth.,* **A243**(1986)348.

12. D. Acosta et al., SPACAL, *Nucl. Instr. and Meth.,* **A294**(1990)193.

13. T. Doke et al., *Nucl. Instr. Meth.,* **A237**(1985)475.

14. D. J. Graham and C. Seez, CMS Note 1996/002 (1996).

15. D. Fournier and L. Serin, p. 291, 1995 European School of High Energy Physics, CERN 96-04, 1996, eds. N. Ellis and M. Neubert.

16. D. Groom, To appear in Proc. of Intl. Conf. On Calorimetry in High Energy Physics, Tucson, 1998.

17. R. Wigmans, *Nucl. Instr. and Meth.,* **A259**(1987)389.

18. G. Drews et al., *Nucl. Instr. and   Meth.,* **A290**(1990)335 and H. Tiecke (ZEUS Calorimeter Group) *Nucl. Instr. and Meth.,* **A277**(1989)42.

19. A. Beretvas et al., CMS TN/94-326 (1994).

20. R. Apsimon et al., *Nucl. Instr. and Meth.,* **A305**(1991)331.

21. A. Annenkov et al., CMS NOTE 1998/041 and references therein.

22. G. Gratta et al., *Ann. Rev. Nucl. Part. Sci.* **44**(1994)453.

23. J. P. Peigneux et al., *Nucl. Instr. and Meth.,* **A378**(1996)410.

24. E. Auffray et al., *Nucl. Instr. and Meth.,* **A412**(1998)223.

25. F. Pauss, these proceedings.

26. M. A. Akrawy et al., *Nucl. Instr. and Meth.,* **A290**(1990)76.

27. D. Fournier, *Nucl. Instr. and Meth.,* **A367**(1995)5.

28. D. Schinzel, Proc. of Intl. Wire Chamber Conference, Vienna, 1998.